Inorganica Chimica Acta 552 (2023) 121505

Contents lists available at ScienceDirect

Inorganica Chimica Acta

journal homepage: www.elsevier.com/locate/ica

New palladium (II) complexes from halogen substituted Schiff base ligands: Synthesis, spectroscopic, biological activity, density functional theory, and molecular docking investigations

Ibrahim Waziri [a,*], Tunde L. Yusuf [b,c,*], Hauwa A. Zarma [d], Samson O. Oselusi [e], Louis-Charl C. Coetzee [f], Adedapo S. Adeyinka [f]

[a] Department of Pure and Applied Chemistry, University of Maiduguri, P.M.B. 1069, Maiduguri, Borno State, Nigeria
[b] Department of Chemical Sciences, University of Johannesburg, Doornfontein, P.O. BOX 17011, 2028 Johannesburg, South Africa
[c] Department of Chemistry, Ekiti State University, P.M.B 5363, Ado Ekiti, Ekiti State, Nigeria
[d] Department of Biochemistry, University of Maiduguri, P.M.B. 1069, Maiduguri, Borno State, Nigeria
[e] School of Pharmacy, University of the Western Cape, Bellville, Cape Town, 7535, South Africa
[f] Department of Chemical Sciences, University of Johannesburg, P.O. Box 524, Auckland Park 2006, South Africa

ARTICLE INFO

Keywords:
Palladium complexes
Anticancer
Antioxidant
Hirshfeld analysis
Molecular docking

ABSTRACT

Two novel palladium (II) complexes **Pd(L1)$_2$** and **Pd(L2)$_2$** derived from *ON* donor bidentate ligands: 2-(((2-bromo-4-chlorophenyl)imino)methyl)phenol (**HL1**) and 2-(((-bromo-4-methylphenyl)imino)methyl)phenol (**HL2**) are reported. The structures of the complexes are unequivocally established using ^{1}H NMR, ^{13}C{H}NMR, Fourier transform-infrared, UV–Vis, TGA, elemental analysis (CHN), mass spectrometry (HRMS), and single crystal X-ray diffraction (SCXRD). The SCXRD revealed that the complexes crystallized as a monoclinic system in *P2(1)/c* space group, in which two ligands coordinated to one Pd(II) center via oxygen and nitrogen atoms of phenolate and imine in a bidentate fashion, resulting in a square planar geometry. The ligands and their complexes were tested for anticancer activity against breast cancer (MCF-7) and colon cancer (HT-29) cell lines, as well as their toxicity profile on HepG-2, a liver cell line, using MTT assays, and compared to 5-fluorouracil (the control). **Pd(L1)$_2$** was found to be more active and selective than **Pd(L2)$_2$**, and it reduced the cancerous cells' viability by more than 70%. **Pd(L2)$_2$** reduced the viability of MCF-7 and HT-29 cell lines by more than 50%. However, the ligands were unable to reduce cancerous cell viability by more than 40%. Both complexes had no effect on the HepG-2 liver cell line at lower concentrations. The two complexes had higher antioxidant activity against DPPH radicals, with IC_{50} values of 33.16 and 38.40 μgmL^{-1}, respectively, than the ligands, which had IC_{50} values of 50.76 and 60.90 μgmL^{-1}. Hirshfeld surface (HS) analysis was used to investigate the non-covalent interaction (NCI) of the complexes and their ligands. The tendency of a pair of chemical species to form crystal packing interactions is computed, which provides the complexes with good contacts in the crystal packing. The DFT studies were performed for the ligands and their complexes at the M06-2X/6-311G (d,p) and LANL2DZ/6–31 + G (d, p) levels of theory, respectively. The structural characteristics, charges (Mulliken and NPA), global reactivity descriptors, MEP, and dipole moments were investigated using this method. Furthermore, a molecular docking study predicted the interactions in the protein–ligand complex.

1. Introduction

Cancer is one of the most serious public health issues, as well as the world's second leading cause of death after cardiac arrest. [1–3]. According to recent data, approximately 19.3 million new cancer cases and approximately 10 million deaths were recorded worldwide [4]. Huge amounts of manpower and resources are expended, but there are no safe and dependable cancer treatments available [5]. As cancer cases rise at an alarming rate, the search for new anticancer agents and effective cancer treatment methods has taken center stage. The development of

* Corresponding authors at: Department of Chemical Sciences, University of Johannesburg, Doornfontein, P.O. BOX 17011, 2028 Johannesburg, South Africa (T.L. Yusuf).
E-mail addresses: triumph2236@gmail.com (I. Waziri), lewistunde@gmail.com (T.L. Yusuf).

https://doi.org/10.1016/j.ica.2023.121505
Received 6 February 2023; Received in revised form 28 March 2023; Accepted 29 March 2023
Available online 31 March 2023

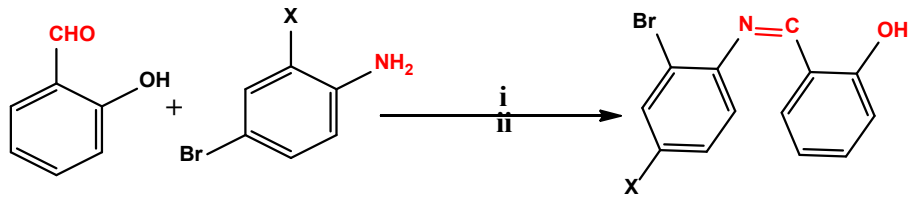

Scheme 1. Synthetic pathways for the preparation of the ligands; i = CH_3OH/HCOOH; ii = RT/3h; X = Cl, **HL1**, and X = CH_3, **HL2.**

anticancer drugs faces significant challenges due to drug resistance and disease relapse. This is a concerning situation because the disease continues to put a strain on global healthcare systems while increasing mortality rates. [6,7].

Several researchers have recently reported the ability of Schiff base-derived complexes to inhibit free radicals as well as various types of cancer cells [8–13]. Because of their diverse biological properties, Schiff base-derived palladium complexes are among the most studied complexes among coordination chemists [14]. Senocak and Akbas, reported that palladium complexes derived from *NO* donor Schiff base ligands as effective DPPH radical scavengers [15]. Also, Palladium complexes of 3-formyl chromone Schiff bases can cleave pUC19 plasmid DNA and scavenge DPPH radicals, according to Kavitha and Laxima [16]. Similarly, Sarto *et al.* discovered that palladium complexes derived from 4-aminoacetophenone Schiff base inhibit MDA-MB-435 cancer cells [17]. We previously synthesized various halogen substituted Schiff base derivatives that demonstrated good antibacterial and radical scavenging activity against Gram-positive and Gram-negative bacteria as well as DPPH radicals [13,18,19]. The presence of halogens increases membrane permeability and molecule absorption [20–22]. Considering the potential of Schiff bases as biomolecules, as well as the broad influence of halogen substituents on these biological properties, we present here the design and synthesis of two novel palladium (II) complexes made of halogen substituted *ON* donor Schiff bases. In vitro antitumor activity was evaluated against human tumor cell lines MCF-7, HT-29, and HepG-2) as well as DPPH radical scavenging activity. The ligands used in this study have previously been reported in our work, and their antimicrobial and antioxidant activities have been assessed [23].

2. Experimental

Materials and instrumentation

All the solvents and chemicals used in this study were of analytical grade and were used exactly as they were received. The elemental compositions of the compounds were estimated using a VarioElementar III microbe CHNS analyzer (carbon, hydrogen, and nitrogen). The palladium content of the complexes was determined using a Spectro Arco FSH12 inductively coupled plasma mass spectrometer. Infrared spectra in the 4000–400 cm^{-1} range were obtained using a Tensor 27 Bruker and Perking Elmer FT-IR spectrometer BX, and electronic absorption spectra in the 800–200 nm range were obtained in acetonitrile at room temperature using a Shimadzu UV–Vis 1800 spectrophotometer. Nuclear magnetic resonance experiment was conducted on a Bruker-500 MHz spectrometer (500 MHz for ^1H and 125 MHz for ^{13}C) using DMSO-d_6 for both proton and carbon analyses, referenced at 2.50 ppm and 39.50 ppm, respectively. A Bruker Apex DUO equipped with a 4 K CCD diffractometer area detector system (at 4 cm from the crystal), a graphite monochromator, a Mo-Kα fine-focus sealed tube (λ = 0.71073 Å), operating at 1.35 kW power were used to obtain single crystal X-ray intensity measurements. The temperature of the samples was maintained at 173 (2) K using an Oxford 700 + series cryostream cooler. Mass spectra were obtained using high resolution mass spectrometry on a WatersAcquity UPLC Synapt G2HD instrument.

2.1. General procedure for the synthesis of the ligands

The ligands were synthesized *via* condensation reaction between 2-hydroxybenzaldehyde and substituted primary amines, following our previous literature procedure [13,24]. In brief, a solution of 2-hydroxybenzaldehyde (1.22 g, 10 mmol, 1 eq) in methanol 20 mL was reacted with solutions of substituted primary amines, namely: 2-bromo-4-chloroaniline (2.05 g, 10 mmol, 1 eq), and 2-bromo-4-methylaniline (1.90 g, 10 mmol, 1 eq) each in 20 mL of methanol in a separate reaction flask. Three drops of formic acid were added, and the resulting mixture was stirred at room temperature for 3 h. The precipitate obtained were filtered, washed with methanol (3 × 10) mL, followed by ether (3 × 10) mL, and dried in a vacuum to afford **HL1** and **HL2** (Scheme 1).

2.1.1. 2-(((2-bromo-4-chlorophenyl)amino)methyl)phenol (HL1)

Yield = 2.48 g, 80.30%; yellow solid; m.p. 165–170 °C; ^1H NMR (500 MHz, DMSO-d_6): δ_H (ppm): 6.96–7.01 (m, 2H, *J* = 7.5 Hz, Ar-H),

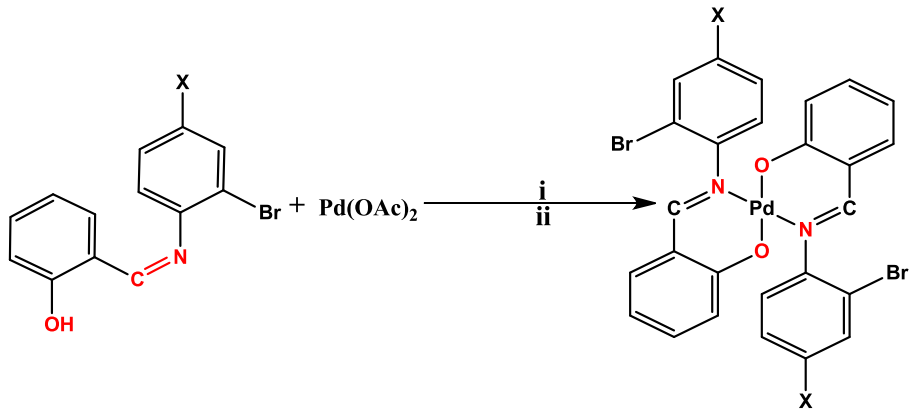

Scheme 2. . Synthetic pathways for the preparation of the complexes; i = CH_3OH/CH_2Cl_2; ii = RT/3h; X = Cl, **Pd(L1)$_2$**, and X = CH_3, **Pd(L2)$_2$.**

7.44–7.47 (m, 1H, $J = 7.0$ Hz, Ar-H), 7.53–7.59 (m, 2H, $J = 8.5$ Hz, Ar-H), 7.66 (d, 1H, $J = 7.0$ Hz, Ar-H), 7.85 (d, 1H, $J = 7.0$ Hz, Ar-H), 8.93 (s, 1H, HC = N), 12.85 (s, 1H, OH);^{13}C{H}NMR (125 MHz, DMSO-d_6): δ_C (ppm): 165.1 (C-OH), 160.5 (HC = N), 145.3, 134.3, 133.3, 132.2, 131.8, 129.2, 121.2, 120.1, 119.6, 119.2, 116.9 (Ar-C); IR:ν_{max}/cm^{-1}: $\nu_{(O—H)} = 3350$, $\nu_{(C=N)} = 1620$, $\nu_{(C—N)} = 1340$, $\nu_{(C\text{-}Cl)} = 820$, $\nu_{(C\text{-}Br)} = 620$; UV–Vis: (ACN, 10^{-3}M): λ_{max}/nm: 214 ($\pi \rightarrow \pi^*$), 273 ($\pi \rightarrow \pi^*$), 345 (n $\rightarrow \pi^*$); CHN Anal. Calculated for $C_{13}H_9BrClNO$; C, 50.27; H, 2.92; N, 4.51; found: C, 50.26; H, 2.90; N, 4.52; HRMS-ESI, m/z [M + H]$^+$: Calculated for $C_{13}H_9BrClNO$, = 309.9634; Found = 309.9680.

2.1.2. 2-(((2-bromo-4-methylphenyl)amino)methyl)phenol (HL2)

Yield = 2.23 g, 77.2%; yellow solid; m.p. 152–156 °C; ^{1}H NMR (500 MHz, DMSO-d_6): δ_H (ppm): 6.97 (t, 2H, $J = 8.5$ Hz, Ar-H), 7.24 (d, 1H, $J = 8.0$ Hz, Ar-H), 7.42 (t, 2H, $J = 8.5$ Hz, Ar-H), 7.48 (d, 1H, $J = 7.5$ Hz, Ar-H), 7.62 (d, 1H, $J = 7.5$ Hz, Ar-H), 8.90 (s, 1H, HC = N), 13.16 (s, 1H, OH); ^{13}C{H}NMR (125 MHz, DMSO-d_6): δ_C (ppm): 163.6 (C-OH), 160.2 (HC = N), 143.2, 138.5, 133.5, 133.0, 132.8, 129.5, 119.34, 119.3, 119.1, 119.0, 116.6 (Ar-C); IR: ν_{max}/cm^{-1}: $\nu_{(O—H)} = 3100$, $\nu_{(C=N)} = 1610$, $\nu_{(C—N)} = 1320$, $\nu_{(C\text{-}Br)} = 780$; UV–Vis: (ACN, 10^{-3}M): λ_{max}/nm: 231 ($\pi \rightarrow \pi^*$), 273 ($\pi \rightarrow \pi^*$), 341 (n $\rightarrow \pi^*$); CHN Anal. Calculated for $C_{14}H_{12}BrNO$; C, 57.95; H, 4.83; N, 4.79; found: C, 57.93; H, 4.82; N, 4.77; HRMS-ESI m/z [M + H]$^+$: Calculated for $C_{14}H_{12}BrNO$, = 290.0181; Found = 290.0291.

2.2. Procedure for the synthesis of the complexes

To synthesize complexes, a solution of palladium (II) acetate (0.11 g, 0.50 mmol, 1 eq) in 10 mL of methanol was added dropwise to the solutions of the ligands: **HL1** (0.31 g, 1 mmol, 2 eq) and **HL2** (0.29 g, 1 mmol, 2 eq) in 20 mL of dichloromethane. The reaction mixture was stirred for 6 h at room temperature, and the green precipitate that formed was collected by filtration, washed with methanol, and dried in a vacuum (scheme 2). Yellow crystals suitable for single-crystal X-ray diffraction analysis were obtained by vapor diffusion of hexane into DCM solution after one week at room temperature.

2.2.1. Bis(2-(((2-bromo-4-chlorophenyl)amino)methyl)phenolato) palladium(II), Pd(L1)$_2$

Yellow crystal; yield, 74.1%; m.p. = 270–274 °C. ^{1}H NMR (500 MHz, DMSO-d_6): δ_H (ppm): 5.92 (d, 1H, $J = 8.5$ Hz, Ar-H), 6.53 (t, 1H, $J = 7.5$ Hz, Ar-H), 7.22 (t, 1H, $J = 7.5$ Hz, Ar-H), 7.42 (d, 1H, $J = 8.0$ Hz, Ar-H), 7.49 (d, 1H, $J = 8.0$ Hz, Ar-H), 7.57 (d, 1H, $J = 6.5$ Hz, Ar-H), 7.88 (s, 1H, Ar-H), 8.08 (s, 1H, HC = N); ^{13}C{H}NMR (125 MHz, DMSO-d_6): δ_C (ppm): 164.7 (C—O), 164.4 (HC = N), 146.3, 135.7, 135.4, 131.1, 130.8, 127.8, 127.6, 120.0, 119.7, 119.6, 119.5, 114.8 (Ar-C); IR: ν_{max}/cm^{-1}: $\nu_{(C=N)} = 1598$, $\nu_{(C—N)} = 1317$, $\nu_{(C\text{-}Cl)} = 840$, $\nu_{(C\text{-}Br)} = 757$; $\nu_{(Pd\text{-}O)} = 543$, $\nu_{(Pd\text{-}N)} = 437$; UV–Vis: λ_{max}/nm: 232 ($\pi \rightarrow \pi^*$), 291 (n $\rightarrow \pi^*$), 421 (MLCT); CHN Anal. Calculated for $C_{26}H_{16}Br_2Cl_2N_2O_2Pd$; C, 43.04; H, 2.22; N, 3.86; Pd, 14.67; Found: C, 43.02; H, 2.22; N, 3.87; Pd, 14.65; HRMS-ESI m/z [M + H]$^+$: calculated for $C_{26}H_{16}Br_2Cl_2N_2O_2Pd$ = 722.8058; Found = 722.8046.

2.2.1.1. Bis(-(((2-bromo-4-methylphenyl)amino)methyl)phenolato)palladium(II), Pd(L2)$_2$.

Yellow crystal; yield, 64.5%; m.p. = 253–256 °C. ^{1}H NMR (500 MHz, DMSO-d_6): δ_C (ppm): 2.38 (s, 3H, CH_3), 5.90 (d, 1H, $J = 8.5$ Hz, Ar-H), 6.49 (t, 1H, $J = 7.0$ Hz, Ar-H), 7.17 (t, 1H, $J = 7.5$ Hz, Ar-H), 7.27 (d, 2H, $J = 7.5$ Hz, Ar-H), 7.40 (d, 1H, $J = 7.5$ Hz, Ar-H), 7.55 (s, 1H, Ar-H), 8.00 (s, 1H, HC = N); ^{13}C{H}NMR (125 MHz, DMSO-d_6): δ_C (ppm): 164.5 (C—O), 164.4 (HC = N), 144.8, 137.5, 135.2 (2C), 131.8 (2C), 128.1, 119.7, 119.6, 114.5 (2C) (Ar-C), 20.1 (CH_3); IR: ν_{max}/cm^{-1}: $\nu_{(C=N)} = 1592$, $\nu_{(C—N)} = 1324$, $\nu_{(C\text{-}Br)} = 757$, $\nu_{(Pd\text{-}O)} = 554$, $\nu_{(Pd\text{-}N)} = 465$; UV–Vis: λ_{max}/nm: 245 ($\pi \rightarrow \pi^*$), 290 (n $\rightarrow \pi^*$), 418 (MLCT); CHN Anal. Calculated for $C_{28}H_{22}Br_2N_2O_2Pd$; C, 49.12; H, 3.24; N, 4.09; Pd, 15.54; Found: C, 49.11; H, 3.22; N, 4.07; Pd, 15.52; HRMS-ESI m/z [M + H]$^+$: calculated for $C_{28}H_{22}Br_2N_2O_2Pd$ = 682.9150; Found = 682.9158.

2.3. X-ray crystallographic analysis

Single crystal X-ray diffraction analysis of the complexes was carried out on a Bruker Smart APEXII diffraction with Mo Kα radiation (I = 0.71073 Å) equipped with an Oxford cryostream low-temperature apparatus operating at 100 K. Data on reflection was collected from various angles, and the APEXII program suite was used to index the reflection [25]. Using narrow frame algorithm software, the frames were integrated with the Bruker SAINT Software package [26].Data were corrected for absorption effects using a multi-scan method (SADABS) [9]. The structure was solved directly with the SHELXS program and refined with the SHELXL program. [12]. Graphics of the crystal structures were drawn using Mercury software [27]. Non-hydrogen atoms were refined isotropically first, then anisotropically using the full-matrix least square method based on F^2 and SHELXL. All hydrogen atoms were geometrically positioned, allowed to ride on their parent atoms, and isotropically refined.

2.4. Hirshfeld surface

Hirshfeld surfaces along with two-dimensional fingerprint plots were calculated using Crystal explorer 17.5 software by loading CIF files as input files at the B3LYP/6-31G(d,p) level of theory [28]. High resolution and d_{norm} functions were used in the generation of the Hirshfeld surfaces of the compounds. The same program was used to create the 2D fingerprint plots. The colour scale for the d_{norm} surfaces is fixed from 0.701 (red) to 1.798 a.u (blue). By including reciprocal touch and translating the range from 0.6 to 2.6 Å, the 2D fingerprints are displayed.

2.5. Antioxidant study

A DPPH radical scavenging assay was used to assess the antioxidant activity of the free ligands and their complexes [29]. In brief, the DPPH radical stock solution (0.1 mM) was prepared in methanol, and 3 mL of the stock was mixed with 1 mL of the compound solutions in DMSO of various concentrations (20–60 μgmL^{-1}). The mixture was incubated in a dark room for 30 min, absorbance was measured using spectrophotometer at a wavelength of 517 nm. The measurements were carried out in triplicates. Ascorbic acid was used as positive control, and the percentage scavenging ability of the compounds was estimated according to the equation:

$$\%SC = [(Ao - Ai)/Ao) \times 100]$$

where % SC = percentage scavenging, A_o = absorbance of the DPPH in methanol, and A_i = absorbance of the tested compounds with the DPPH in methanol.

2.6. Cytotoxicity study

The cyto-toxic effect of the free ligands and their complexes against (MCF-7 breast cancer cell line and HT-29 colon cancer cell line), and (HepG-2 liver cell line) was assessed *in vitro* using MTT assay. 5-Fluorouracil and untreated cells were included in the experiment as positive and negative control, respectively. The cells were cultured in sterile Dulbecco's Minimal Essential Medium (DMEM, Gibco) supplemented with 10% Fetal bovine serum (FBS) and 1% penicillin–streptomycin solution and incubated for 24 h at 37 °C in 5% CO_2. After the cells reached 80% confluence, they were harvested using a 2% trypsin-EDTA solution, centrifuged for 5 min at 3000 rpm, and re-suspended in DMEM. Cell counting was done using a handheld automated cell counter (Scapter 3.0^{TM}, Merck, Burlington, MA, USA), and 1 × 10^4 cells/well were seeded into 96-well plates, incubated for 24 h, and treated with

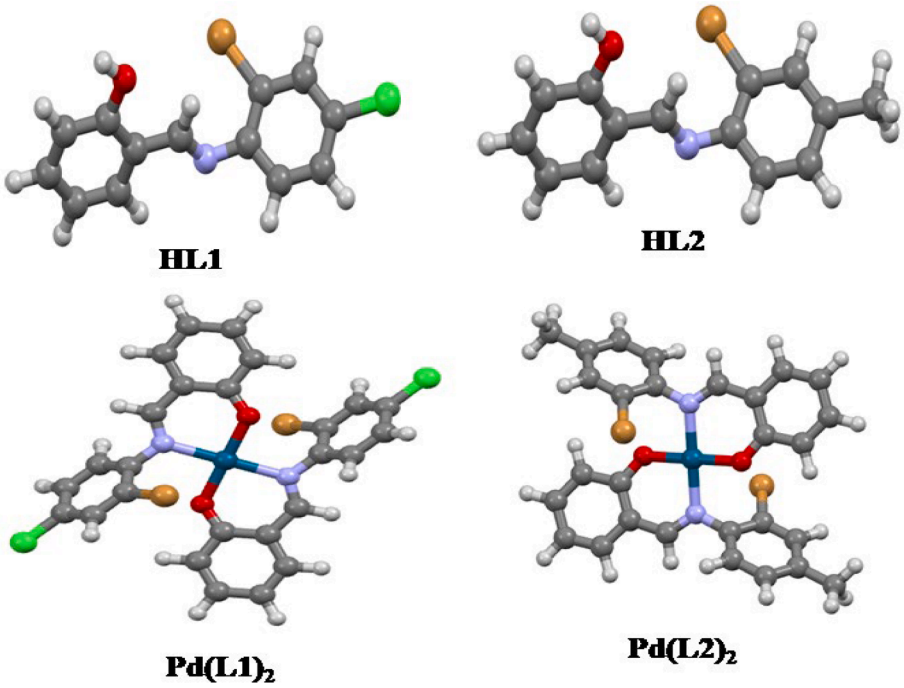

Fig. 1. Optimized structures of ligands and their complexes.

different concentrations (10, 25, 50, and 100 gmL^{-1}) of the test compounds. The MTT solution (20 μL) prepared in PBS (5 $mgmL^{-1}$) was added to all the wells and the plates were incubated for another 4 h, followed by 1 h incubation with 100 μL of dimethyl sulfoxide (DMSO) to dissolve the formazan crystals. All experiments were performed in triplicate. The plates were read at 570 nm at a reference wavelength of 630 nm using an ELISA plate reader (Varioskan Flash, ThermoFisher Scientific, Vanta, Finland). The percentage of cell viability was calculated using the following formula.

$$Cellviability(\%) = \frac{At}{Ab} \times 100$$

where, A_t represents the absorbance value of the test compound, and A_b, the Absorbance value of the blank. The IC_{50} values, i.e., the concentration of the drug that inhibits 50% of the cells were obtained from dose–response curves and comparisons were assessed by one-way ANOVA performed using GraphPad Prism 5.0 (GraphPad Software Inc., San Diego, CA, USA). The data were expressed as means ± SD.

2.7. Theoretical study

For ligands, the M06-2X/6-311G(d,p) level of theory [30] was selected, while for the complexes, the LANL2DZ/6–31 + G(d,p) level of theory [31] was selected to perform DFT calculations using Gaussian 09 software [32]. The polarizable continuum model (PCM) [33] was used to characterize solvation effects by optimizing the geometries of each component in MeOH. The optimized structures were combined with frequency calculations to determine if they achieved their minimum conformation energies, yielding the structures shown in Fig. 1. The optimized structures were then used as input for quantum theory of atoms in molecules (QTAIM) analysis, which involved using multiwfn [34] and vmd [35] software to reveal molecular electrostatic potentials (MEP) and to execute conceptual density functional theory (CDFT) calculations and analysis, as well as to reveal non-covalent interactions (NCI). The NCI index is a method that analyzes the regions of weak electron density and low electron density gradients and can detect NCI below the QTAIM analysis identification threshold [36]. MEP and CDFT are chemical descriptors that use electron densities to determine the reactive sites in compounds [37,38].

2.8. Molecular docking study

In this study, a computer-based docking technique was used to hypothetically evaluate the binding affinity of the synthesized compounds to MCF-7 and HT-29 proteins. The X-ray crystal structure of representative protein targets was downloaded from the RCSB Protein Data Bank web server (https://www.RCSB.org) [39]. ChemDraw Ultra 0.7 was used to create the two-dimensional structures of the compounds, which were subsequently converted to MOL2 format using the Open Babel 2.4.1 program [40]. The ligands and target were prepared on the PyRx software program (version 0.8) installed on a Windows 10 ultimate PC with an Intel Core i5-7200U processor, 8 GB of memory, and a 64-bit operating system. The docking area was chosen by creating a grid box with a size of 25 Å and the coordinates of the proteins were set as follows: MCF-7 (x = 83.40, y = 50.11 and z = 46.42) and HT-29 (x = 33.78, y = 34.24 and z = 3.82). Thereafter, the docking calculations were performed by the Lamarckian genetic algorithm using the built-in AutoDock Vina widget on the PyRx program [41,42]. Finally, the results were analyzed and the poses with the lowest binding affinity were visualized for the formation of various types of interactions using the BIOVIA Discovery Studio Visualizer software (v21.1.0).

3. Results and discussion

3.1. Physical characterizations

The reaction pathways for the synthesis of the ligands and their complexes are shown in Schemes 1–2. The ligands and their complexes were obtained in moderate yields (65–80%). The complexes were found to be non-hygroscopic, air-stable, and soluble in acetonitrile, chloroform, and dimethyl sulfoxide. The melting points of the complexes were found to be higher than the ligands, which could be due to the increase in the size of the molecules and also the presence of ionic and coordinate bonds between the oxygen and nitrogen atoms of the ligands and the Pd (II) ion. The result of the elemental (CHN) analysis of the ligands and their complexes agrees with the theoretical values.

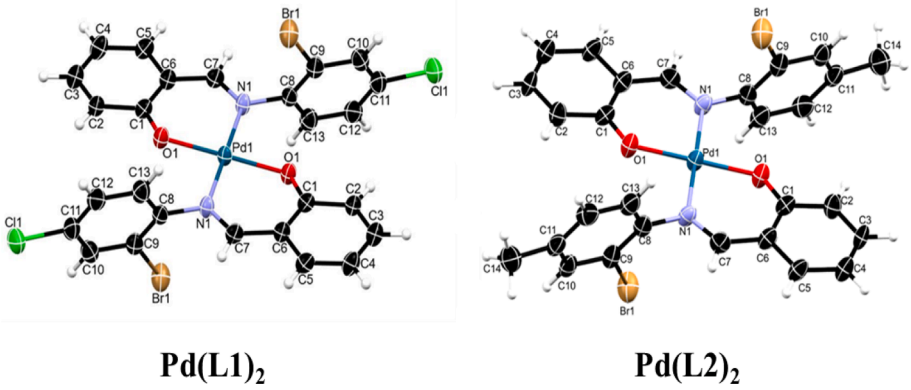

Fig. 2. Crystal structures of complexes.

Table 1
Crystal data and structure refinement for the complexes.

Identification code	$Pd(L1)_2$	$Pd(L2)_2$
Empirical formula	$C_{26}H_{16}Br_2Cl_2N_2O_2Pd$	$C_{28}H_{22}Br_2N_2O_2Pd$
Formula weight	721.80	681.91
Temperature/K	100.00	100.00
Crystal system	monoclinic	monoclinic
Space group	P2(1)/c	P2(1)/c
a/Å	10.621(3)	10.6949(14)
b/Å	9.820(2)	9.7100(12)
c/Å	12.594(4)	12.7714(17)
α/°	90	90
β/°	107.275(11)	106.985(6)
γ/°	90	90
Volume/Å^3	1254.3(6)	1268.4(3)
Z	2	2
ρ_{calc}g/cm^3	1.921	1.793
μ/mm^{-1}	4.166	3.910
F(000)	704.0	672.0
Crystal size/mm^3	0.147 × 0.082 × 0.02	0.138 × 0.132 × 0.024
Radiation	MoKα (λ = 0.71073)	MoKα (λ = 0.71073)
2Θ range for data collection/°	4.016 to 56.756	3.982 to 56.74
Index ranges	$-14 \le h \le 14$, $-13 \le k \le 13$, $-16 \le l \le 16$	$-14 \le h \le 14$, $-12 \le k \le 12$, $-16 \le l \le 16$
Reflections collected	19,705	19,277
Independent reflections	3125 [R_{int} = 0.0964, R_{sigma} = 0.0605]	3149 [R_{int} = 0.1100, R_{sigma} = 0.0781]
Data/restraints/parameters	3125/0/160	3149/0/161
Goodness-of-fit on F^2	1.051	1.035
Final R indexes [I>=2σ (I)]	R_1 = 0.0478, wR_2 = 0.1152	R_1 = 0.0532, wR_2 = 0.1243
Final R indexes [all data]	R_1 = 0.0778, wR_2 = 0.1297	R_1 = 0.1018, wR_2 = 0.1483
Largest diff. peak/hole / e Å^{-3}	2.15/-0.95	1.81/-1.59

Table 2
Selected bond parameters for complexes.

Bond parameters	$Pd(L1)_2$ [theoretical]	$Pd(L2)_2$ [theoretical]
Bond distances		
Pd^1-O^1	1.980(3)[2.025]	1.971(4)[2.026]
Pd^1-O^{11}	1.980(3)[2.025]	1.971(4)[2.026]
Pd^1-N^1	2.012(4)[2.077]	2.013(5)[2.078]
Pd^1-N^{11}	2.012(4)[2.077]	2.013(5)[2.078]
Br^1–C^9	1.884(6)[1.889]	1.883(6)[1.895]
O^1-C^1	1.308(6)[1.300]	1.298(7)[1.300]
N^1-C^7	1.297(6)[1.295]	1.289(8)[1.293]
N^1-C^8	1.435(6)[1.419]	1.436(7)[1.421]
Bond Angles		
O^1–Pd^1-O^{11}	180.0[180.0]	180.0[179.98]
O^1-Pd^1-N^1	91.89(15)[90.67]	92.40(18)[89.55]
O^1-Pd^1-N^{11}	88.11(15)[89.33]	87.60(19)[89.55]

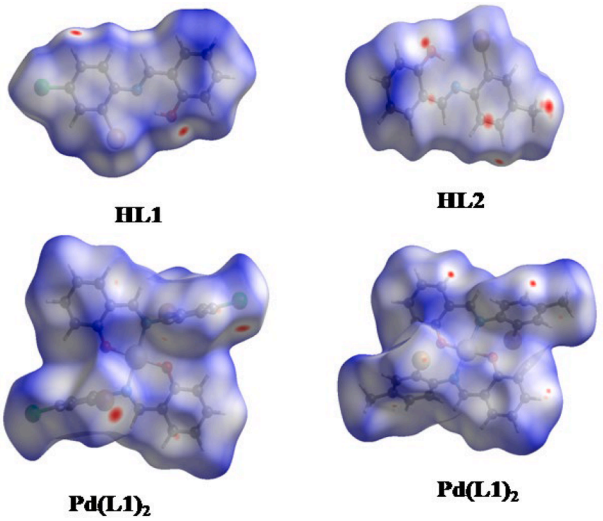

Fig. 3. Hirshfeld surface mapped with dnorm for visualizing the intermolecular interactions of the ligands and their complexes.

3.2. Description of crystal structure of the complexes

Single crystals of **Pd(L1)$_2$** and **Pd(L2)$_2$** were obtained by vapor diffusion of hexane into DCM solution after three days as yellow blocks. The pictorial representation of complexes is presented in Fig. 2, with selected crystallographic and bond parameters around the metal center in Tables 1 and 2, respectively. Both complexes crystallized in a monoclinic space group, P2(1)/c, with similar coordination mode and geometry. The asymmetric units of both complexes had half of the molecules with the Pd center located at the crystallographic center of inversion. The ligand coordinated to the metal center in a bidentate manner with donors from imine nitrogen and phenolate oxygen atoms from the two adjacent ligands. The geometry around the Pd (II) center in both complexes is slightly distorted square planar with bond angles ranging from 88.91(15) to 180.0° and 87.11(19) to 180°, respectively. The bond parameters of the complexes are comparable with similar reported palladium structures [43–49]. For molecular packing in **Pd(L1)$_2$**, the structure is held together by CH•••π (3.717 Å) and halogen bonding interaction between Cl•••Br (3.202 Å) from the neighbouring independent molecules.

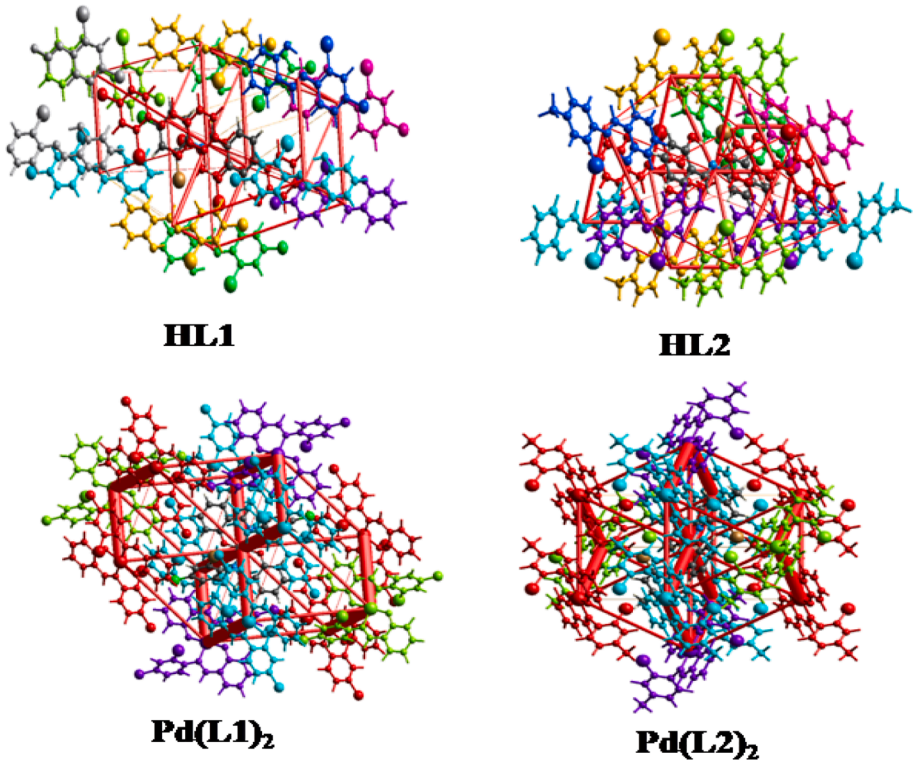

Fig. 4. Coulomb intermolecular interaction topology energy framework between neighbouring molecules within each molecular crystal structure.

3.3. Hirshfeld surface analysis

Hirshfeld surface analysis (HSA) visually represents intermolecular interactions and molecular morphologies in a crystalline environment, which helps investigate packing modes and intermolecular interactions in molecular crystals. Surface characteristics of various types of intermolecular interactions can be identified by color-coding distances from the surface to the next atom exterior (de plots) or interior (di plots) to the surface. It visually depicts the various interactions and demonstrates how each molecule contributes differently to the image [50].

Hirshfeld surfaces (HS) and their associated two-dimensional fingerprint plots were used to reveal the various interactions between the ligands **HL1** and **HL2** and their complexes **Pd(L1)$_2$** and **Pd(L2)$_2$**. These entities show the variations in intermolecular interaction forms and the corresponding contributions to the HS (in percentage). DNM mapping on the molecular HS of the ligand and complexes is shown in Fig. 3, and their respective 2D fingerprint plots are shown in the supplementary information. The bright red spots represent short contacts, the white areas represent the van der Waals separation region, and the blue areas represent no contacts [51,52]. The HS displays the intermolecular interactions using the standard color code. Large, bright red spots indicate strong interactions between neighboring molecules.

The percentage contributions from interactions within the compounds are shown in the two-dimensional fingerprint plots (supplementary information Figs. S29-32). The significant number of contacts in all of these compounds contributed to overall contact surface areas of more than 1%. At first glance, the bright red spots in Fig. 3 appear to indicate percentage contributions of close to 10%. However, the red spots in Pd(L2)$_2$ are significantly less bright than in the other compounds, although it displays more contact surface areas with over 10% more contributions than the other compounds when we evaluated the two-dimensional fingerprint plots. Another significant feature is the large H—H contact surface areas, **HL2**, and Pd(L2)$_2$. Substantial Br…H and H…Br contact surface areas are also observed in these compounds, although they decrease significantly upon complexation from **HL1** to **Pd(L1)$_2$**. Furthermore, an increase in Br…H and H…Br contact surface areas was observed upon complexation from **HL2** to **Pd(L2)$_2$**. A substantial C…C decrease in contact surface areas was observed upon complexation, while substantial increases in C…Br and Br…C contact surface areas were observed in both ligands. Although Br-Br contact surface areas were absent in the ligands, they were observed in the complexes. However, Br…O and O…Br contact surface areas were observed in the ligands but not in the complexes. A similar phenomenon was observed for C…N, N…C, N…O and O…N contact surface areas. Similarly, the opposite phenomenon was observed for the N…H and H…N contact surface areas, as they were observed in the complexes but not in the ligands. A significant increase in the contact surface areas of C…H and H…C was observed upon complexation in both complexes. This confirms the CH•••π molecular packing observed in the Pd(L1)$_2$ crystal structure. The contact surface areas of C…H and H…C also increase from **HL1** to **HL2**. C…O and O…C contract surface areas were found in the ligands but not in the complexes. After complexation, both ligands showed a decrease in O…H and O…H contact surface areas. When the Cl interactions were examined in **HL1** and **Pd(L1)$_2$**, it was discovered that the contact surface areas of C…Cl and Cl…C decrease with complexation. The existence of Cl…Cl contact surface areas was noticed in **HL1** but not in **Pd(L1)$_2$**. Similarly, an increase in the contact surface areas of H…Cl and Cl…H after complexation was seen. The Cl•••Br halogen bonding interaction observed in the crystal structure's molecular packing was confirmed in **Pd(L1)$_2$**, but not in **HL1** (see details in supporting information Fig. S29–32). Similar observations were reported on some palladium complexes [53–55].

For the intermolecular topology network, molecules with the same colour reveal interaction between them in this network (Supplementary information Fig. S33). These colors correspond to symmetry operations (*Sym* op), where R is the distance between molecular centroids (Tables S1-4). In the **HL1** ligand, the strongest interaction is observed at R = 4.62 Å. A substantial interaction is also observed at R = 6.85. In general, there is a correlation between R and Etot, where the latter increases as the former decreases. However, the value of R = 13.25 Å

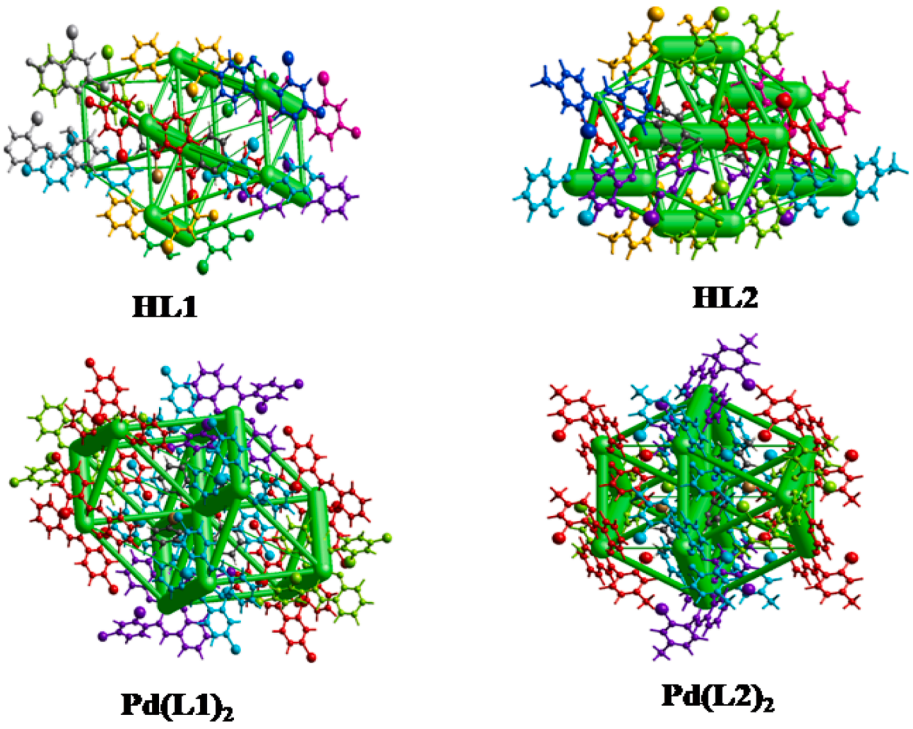

Fig. 5. Dispersion intermolecular interaction topology energy framework between neighbouring molecules within each molecular crystal structure.

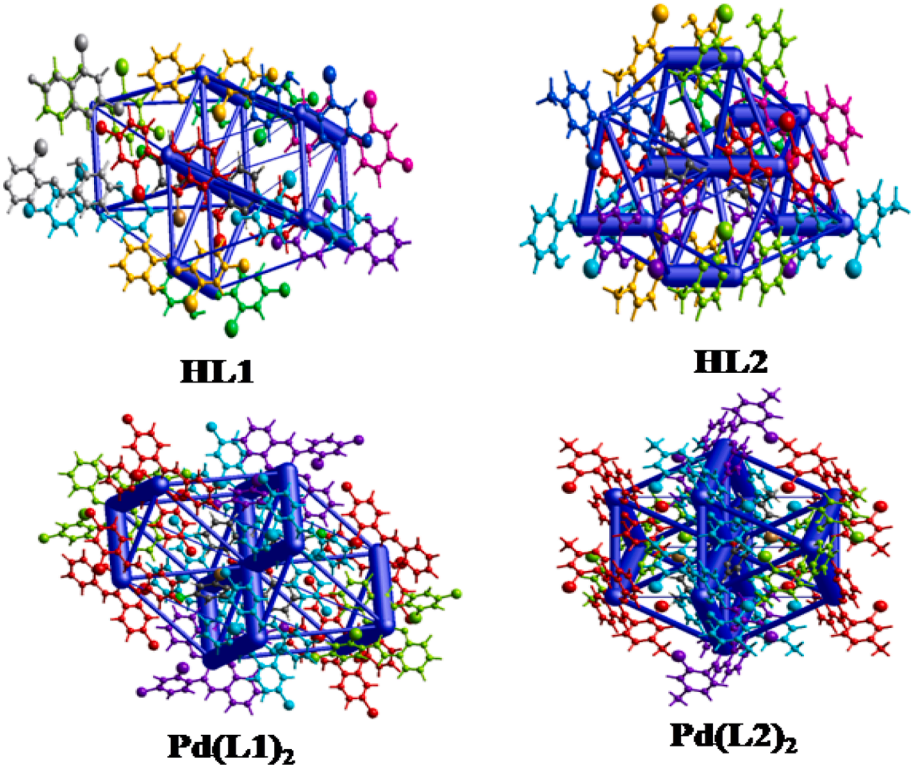

Fig. 6. Total intermolecular interaction topology energy framework between neighboring molecules within each molecular crystal structure.

deviates from this relationship. A similar correlation is observed for **HL2**, with R = 12.07 being an outlier. As in the ligands, a similar correlation is also observed in **Pd(L1)$_2$**, without any outlier. This relationship was also observed in **Pd(L2)$_2$** (see supplementary information Fig. S34). This suggests the existence of stronger interaction energies at shorter distances between molecular centroids. Furthermore, at longer distances between molecular centroids, complexes had more vital interaction energies than ligands (R8 for the former versus R5 for the latter). Because of their preferential binding and selectivity affinities to substrates, **HL1** and **Pd(L1)$_2$**, are more biologically viable than **HL2** and **Pd(L2)$_2$** [56]. For each interacting molecule, a vector property influences the topology of the intermolecular interactions in each crystal

[57,58]. The total energy (Etot) is denoted by eq 1 after a perturbation that causes energy decomposition.

$$E_{tot} = E_{ele} + E_{pol} + E_{dis} + E_{rep} \quad (1)$$

where E_{ele}, E_{pol}, E_{dis}, and E_{rep} represent: electrostatic, polarization, dispersion and repulsive energies, respectively [57]. Figs. 4-6 show the energy framework between the topology network's molecular pairs in each crystal molecule. This framework is built by connecting the interacting atoms between each interacting molecule in the crystal's topology. These interacting atoms are the same as those described earlier in our analysis of the two-dimensional fingerprint plots.

3.4. Infrared spectra

Infrared spectroscopy is useful for identifying the characteristic functional groups and their frequency of vibrations in the free ligand, as well as for verifying evidence of interactions between those groups and the central metal ion [59]. The IR spectra of the free ligands and their complexes (supplemental information) were obtained in the 4000–400 cm^{-1} range to examine the functional groups in the ligands and also to corroborate their interaction with the Pd(II) ion. The appearance of strong peaks at 1610–1620 cm^{-1} in the free ligands, which is assignable to $\nu_{(C=N)}$ vibrational frequency indicated the formation of the Schiff base ligands **HL1** and **HL2**. These peaks were observed at 1592–1598 cm^{-1} in the spectra of the complexes. The shifts of these vibrational frequencies to a lower wave number in the complexes are due to the decrease in electron density on nitrogen atom of imine group as the result of donating a lone pair of electrons to the Pd(II) ion during coordination [60]. Similarly, $\nu_{(O-H)}$ vibrational frequency was observed at 3100–3350 cm^{-1} in the free ligands as a weak band due to intramolecular hydrogen bonding with the nitrogen atom of the imine group. This is in agreement with the values reported by Rajegowda et al., 2022 [61]. These bands were not observed in the spectra of the complexes, thus suggesting deprotonation of the hydrogen atom of the phenolic group and confirming coordination of the phenolate oxygen to the Pd(II) ion in the complexes. The peaks for $\nu_{(C-O)}$ and $\nu_{(C-N)}$ band stretching shifted to lower frequencies in the complexes, affirming the participation of oxygen and nitrogen atoms in the coordination. Similar observation was reported by Muhammad et al., [62]. The appearance of new peaks in the spectra of the complexes that are assignable to $\nu_{(Pd-N)}$ and $\nu_{(Pd-O)}$ vibrational stretching confirmed the involvement of imine nitrogen and phenolic oxygen in the complexes' formation. [63].

3.5. Nuclear magnetic resonance

The spectra of the ligands and their complexes were recorded in DMSO-d_6 as a solvent and are shown in the supplementary material. The chemical shift of the imine (HC=N) proton was observed as a single peak at 8.93 and 8.90 ppm in the ^{1}H NMR spectra of the ligands **HL1** and **HL2**, respectively. After coordination to Pd(II), the peaks in **Pd(L1)$_2$** and **(PdL2)$_2$** shifted to the upfield at 8.08 and 8.00 ppm, respectively. The shielding effect of the Pd(II) ion and conformational change due to chelation could be responsible for the up-field shift of these protons [60,64]. This observation further supported the discussion in the IR section, where the shifting of the imine stretching bands to a lower vibrational frequency was ascribed to the coordination of the nitrogen atom to the Pd(II) ion. Furthermore, the aromatic protons that were observed as multiplets in the spectra of the free ligands were found to be clearly resolved in the complexes, with J_{HH} values of 7.0 and 8.5 Hz, suggesting the presence of ortho aromatic protons. The phenolic (OH) proton signals in the ligands **HL1** and **HL2** were observed at 12.85 and 13.16 ppm, respectively. Upon coordination, these peaks were not observed in the spectra of the complexes, indicating the deprotonation and subsequent coordination of the oxygen atoms to the Pd(II) ion. Similarly, this observation supported the discussion in the IR section,

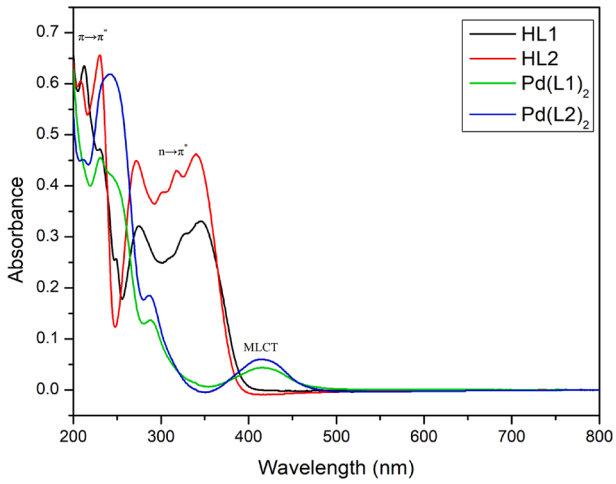

Fig. 7. Electronic absorption spectra of the ligands and their complexes.

where the disappearance of the $\nu_{(O-H)}$ stretching band in the spectra of the complexes was attributed to the deprotonation of the phenolic proton and subsequent coordination of the phenolate oxygen to Pd(II) ion. These findings corroborate those reported by Zeinab *et al.*, [44].

The ^{13}C{H}NMR spectra of the ligands are distinguished by the presence of two peaks in the downfield region at 165.1 and 160.5 ppm and 163.6 and 160.2 ppm, respectively, corresponding to (C-OH) and (C=N) signals for **HL1** and **HL2**. These signals were observed at 164.7 and 164.4 ppm in **Pd(L1)$_2$** and **Pd(L2)$_2$**, respectively, after complexation. This shift is caused by the shielding effect of the Pd(II) ion, which confirms coordination through the oxygen and nitrogen atoms of the phenolate and imine groups. This is similar to what has been reported in related complexes. [65].

3.6. UV–Visible absorption studies

The electronic absorption spectra of the ligands and their complexes were obtained using an acetonitrile (10^{-3} M) solution, and the combined spectra are shown in Fig. 7. The ligands **HL1** and **HL2** showed three absorption bands between 214 and 231 nm, 273 nm, and 341 and 345 nm, respectively. These bands are assignable to the $\pi \rightarrow \pi^*$ and $n \rightarrow \pi^*$ transitions due to C=C and C=N, respectively [66]. After complexation, the bands showed a red shift toward absorption maxima at 232–245 nm and 290–291 nm, as well as a hypochromic effect. This could be due to the structural conformation change caused by coordination to the Pd(II) ion. The bands due to the $n \rightarrow \pi^*$ transition around 341–345 nm, however, disappeared in the complexes, which can be attributed to the transfer of a lone pair of electrons from the imine nitrogen to the Pd(II) ion. Furthermore, between 418 and 421 nm, new broad bands were observed in the spectra of the complexes. This is compatible with MLCT, which allows for the formation of square planar geometry around the Pd (II) ion [67,68], proved by the single crystal X-ray analysis. This is consistent with the electronic spectra of square planar palladium complexes derived from Schiff bases [69,70].

3.7. Mass spectra

The ESI-MS spectra of the ligands **HL1**, **HL2** and their Pd(II) complexes are presented in supplementary information. The spectra of the ligands and their complexes confirmed the stoichiometric structure of the compounds. The spectrum of **HL1** (Fig S7), showed *m/z* signal at 309.9680 for $[M + H]^+$ which corroborates well with the calculated value of 309.9634. The spectrum of **HL2** (Fig S14), gave *m/z* signal at 290.0281 for $[M + H]^+$ and this agreed with the calculated value of 290.0181. The spectrum of **Pd(L1)$_2$** (Fig. S21), presented *m/z* signals at 720.8035, which corresponds to the calculated value of 720.7912, for

Table 3
DPPH radical scavenging activity and IC_{50} of the ligands and their complexes.

Compounds	DPPH scavenging ability (%)					IC_{50}
	20 μgmL^{-1}	30 μgmL^{-1}	40 μgmL^{-1}	50 μgmL^{-1}	60 μgmL^{-1}	
HL1	22.0 ± 0.7	30.2 ± 0.1	38.2 ± 0.07	44.6 ± 0.2	62.8 ± 0.3	50.76
HL2	15.6 ± 0.3	22.3 ± 0.3	31.5 ± 0.1	37.5 ± 0.3	54.6 ± 0.5	60.90
$Pd(L1)_2$	43.5 ± 0.6	54.8 ± 0.09	61.2 ± 0.3	66.4 ± 0.09	75.4 ± 0.08	33.16
$Pd(L2)_2$	37.6 ± 0.1	48.4 ± 05	57.3 ± 0.4	62.4 ± 0.7	68.5 ± 0.6	38.40
AA	55.1 ± 0.9	68.4 ± 0.2	75.3 ± 0.08	87.5 ± 0.06	94.2 ± 0.3	27.79

AA = Ascorbic acid (control).

Table 4
IC_{50} values of the ligands, complexes and the control drug on the cancer cell lines.

Compounds	IC_{50} values (μgmL^{-1})		
	MCF-7	HT-29	HepG-2
HL1	62.4	70.8	–
HL2	111.7	117.5	–
$Pd(L1)_2$	21.5	15.3	47.6
$Pd(L2)_2$	38.5	35.3	54.4
5-Fu	6.5	8.7	41.6

(–) = not applicable.

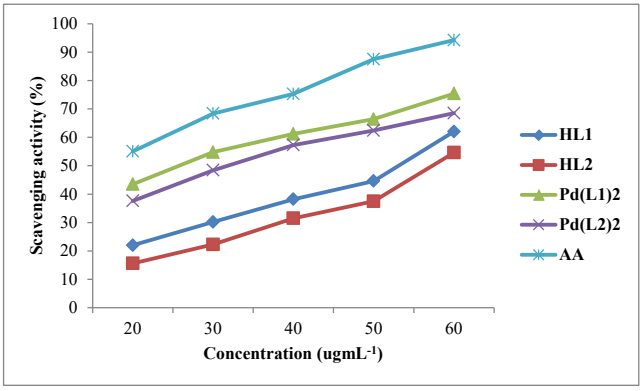

Fig. 8. DPPH radical scavenging activity of the ligands and their complexes.

$[Pd(L1)_2 + H]^+$. Similarly, the spectrum of **$Pd(L2)_2$** (Fig. S28), displayed *m/z* signals at 682.9158 for $[Pd(L2)_2 + H]$, which agrees 682.9161. Additional peaks with *m/z* values that match to the two different bromine isotopes (^{79}Br and ^{81}Br) were also observed in the spectra of the ligands and their complexes.

3.8. Thermogravimetric analysis

TGA was performed on the ligands and their complexes at temperatures ranging from 25 to 800 °C, and the thermograms are shown in the supplementary material. Both the ligands and their complexes lost weight gradually as temperature increased, indicating fragment decomposition. **HL1** is stable at temperatures ranging from 25 to 250 °C before decomposition, with a weight loss of 99.34%. However, **HL2** was stable before decomposition within the temperature range of 25–275 °C, with a weight loss of 99.12%. The complete decomposition of the ligands at a specific temperature without any residual further confirmed the ligands' high purity as demonstrated by HRMS and NMR. The complexes exhibited similar patterns with minor differences from the ligands. All the complexes showed stability up to 300 °C before gradual decomposition. These decomposition pattern steps represent the loss of the ligands and subsequent formation of PdO. In general, the complexes demonstrated higher thermal stability than the ligands.

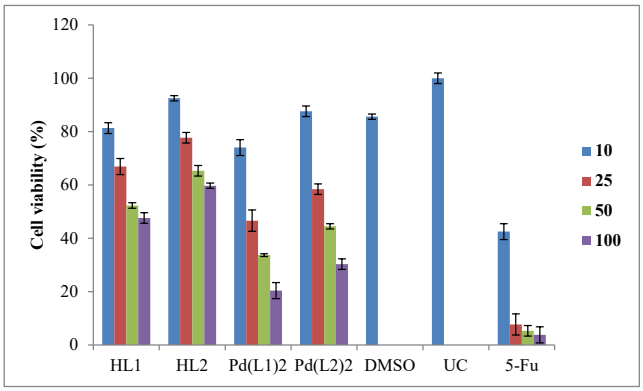

Fig. 9. Viability of MCF-7 cell lines (% in relation to control) after treatment with different concentration of the ligands and their complexes. Control = untreated cells in 10% DMSO. UC = untreated cells, 5-Fu = 5-Fluorouracil. DMSO included as a control due to its use a solvent carrier for the test compounds.

3.9. Biological study

3.9.1. Antioxidant activity

The antioxidant potentials of the ligands and their complexes were investigated in comparison to ascorbic acid (control) using the DPPH radical scavenging assay, and the results are shown in Table 3 and Fig. 8. The results show that the complexes have higher radical scavenging activity than their respective ligands but are lower than the control. Table 3 shows that the scavenging activity of both ligands and their complexes is concentration dependent. Despite their similar structures, the presence of different substituents influences their radical scavenging activity. The multiple electron withdrawal group on **HL1** improved its scavenging activity against **HL2**, which has a combination of electron withdrawal and electron donating groups. Halogens substituents are known to enhances the biological activity of Schiff bases and their complexes due to their ability toward increasing membrane permeability and absorption [22]. This is responsible for the variation in the scavenging activity of the ligands. Similar observations were reported by Anu and co-workers. [71]. It can be observed that **HL1** has an IC_{50} of 50.76 40 μgmL^{-1}, while **HL2** shows an IC_{50} of 60.90 40 μgmL^{-1} (Table 3). Similarly, $Pd(L1)_2$ shows higher radical scavenging activity than **$Pd(L2)_2$**. The complexes show IC_{50} values of 33.16 and 38.40 μgmL^{-1}, respectively (Table 3). In general, both complexes demonstrated promising radical scavenging activity compared to their free ligands. This result is in agreement with the previous studies on the antioxidant activity of palladium complexes derived from Schiff bases [15,72,73]. The complexes' higher radical scavenging activity is due to Pd(II)'s ability to provide a d^8 system that is electron rich at the metal center and could increase the electron density around the ligand after complexation, resulting in increased radical scavenging [74]. The finding that Schiff bases, despite having a phenolic functional group, had less radical scavenging activity than their Pd(II) complexes supported the role of the metal center in complex biological properties. Nizam and colleagues also reported a palladium complex derived from a tetradentate ligand. The study demonstrated that, despite the phenolic moiety of the ligand, it could not outperform the complex in terms of radical scavenging activity. This supports the role of the metal center in complex biological properties [75].

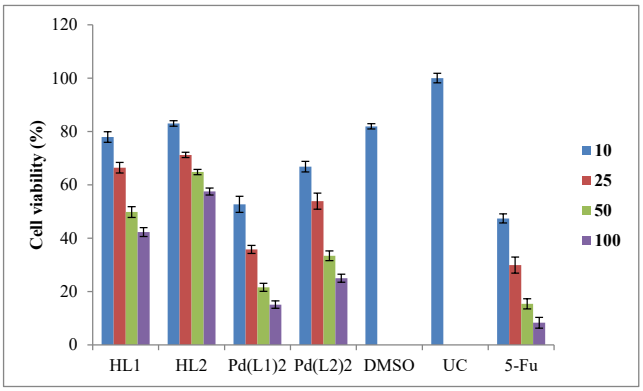

Fig. 10. Viability of HT-29 cell lines (% in relation to control) after treatment with different concentration of the ligands and their complexes.

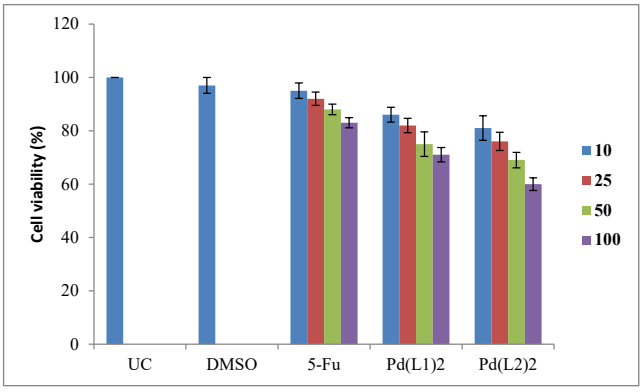

Fig. 11. Viability of HepG-2 cell lines (% in relation to controls) after treatment with different concentration of the complex.

3.9.2. *Cyto-toxicity study*

The cytotoxicity of the ligands and their complexes was evaluated on cancerous cell lines. These include the breast cancer cell line MCF-7 and the colon cancer cell line HT-29. The activity of the compounds and the control drug against the tested cell lines is expressed in terms of cell viability and IC_{50} after 48 h of exposure. The results are presented in Figs. 9–11 and Table 4. The cytotoxicity of the compounds increases with increased concentration. Furthermore, the complexes induced more toxicity than their respective ligands but less than the control drug. **Pd(L1)$_2$** shows higher toxicity against both cell lines than **Pd(L2)$_2$** and reduces the cell viability by more than 70% at a concentration of 100 μgmL^{-1}. **(PdL2)$_2$** only reduced the cell viability by 65% at the same concentration (Figs. 9–10). The IC_{50} of the ligands HL1 and HL2 was found to be 62.4 and 70.8 μgmL^{-1} and 111.7 and 117.5 μgmL^{-1} on MCF-7 and HT-29, respectively. The complexes **Pd(L1)$_2$** and **Pd(L2)$_2$** have IC_{50} of 21.5 and 15.3 μgmL^{-1} and 38.5 and 35.3 μgmL^{-1} for MCF-7 and HT-29 respectively, Table 4. The marked increase in cyto-toxic activity of **HL1** and **Pd(L1)$_2$** over **HL2** and **Pd(L2)$_2$** could be explained based on their structural differences. The presence of multiple electrons withdrawing substituents in these compounds is responsible for their higher activity against **HL2** and its corresponding complex that has a combination of electron withdrawing and donating substituents. Electron withdrawing group enhances the interaction between the compound and the receptor from the target. Kayed et al. discovered that the presence of electron-withdrawing group substituents improves the biological properties of palladium complexes [76].

The complexes were also tested for toxicity against HepG-2 liver cell lines, the results of which are shown in Fig. 11. At lower concentrations, the complexes had negligible toxicity to the cells. The cells-maintained viability of 80% or higher after treatment with **Pd(L1)$_2$** at 10 and 25 μgmL^{-1}, and 71 and 75% at 50 and 100 μgmL^{-1}, respectively. When cells were exposed to **Pd(L2)$_2$**, their viability was 81% at 10 μgmL^{-1} and 76, 69, and 60% at 25, 50, and 100 μgmL^{-1}, respectively. Furthermore, at lower concentrations, the standard drug resulted in cell viability of 95–92% and at higher concentrations, cell viability of 88–83%. Statistical analyses (a student's *t*-test with a 95% confidence interval) revealed no significant difference between the treated cells and the control at lower concentrations, confirming the complexes' low toxicity

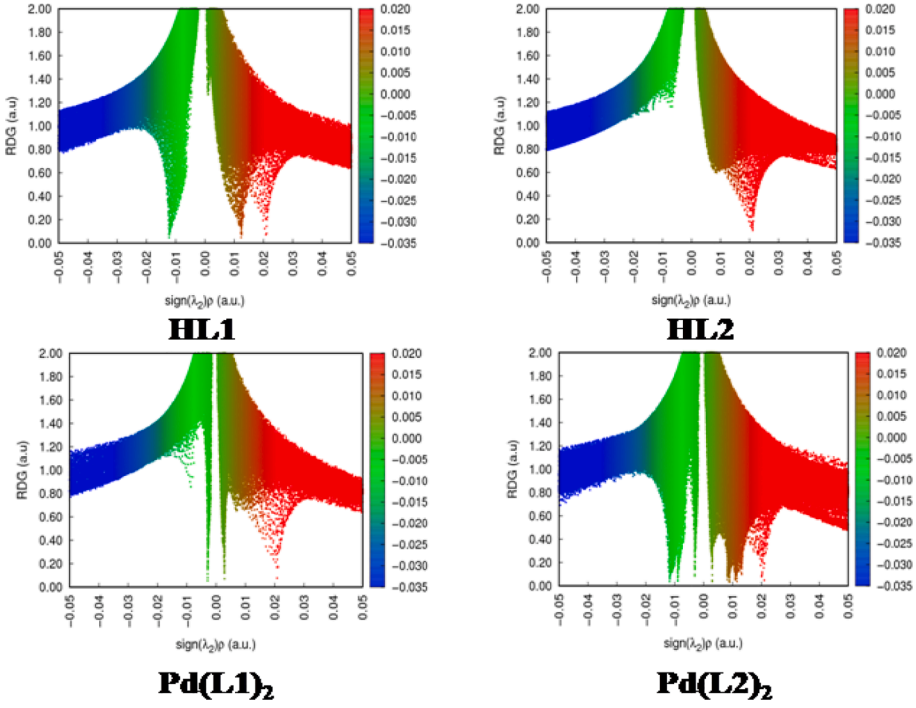

Fig. 12. Two-dimensional reduce density gradient plots for ligands and complexes.

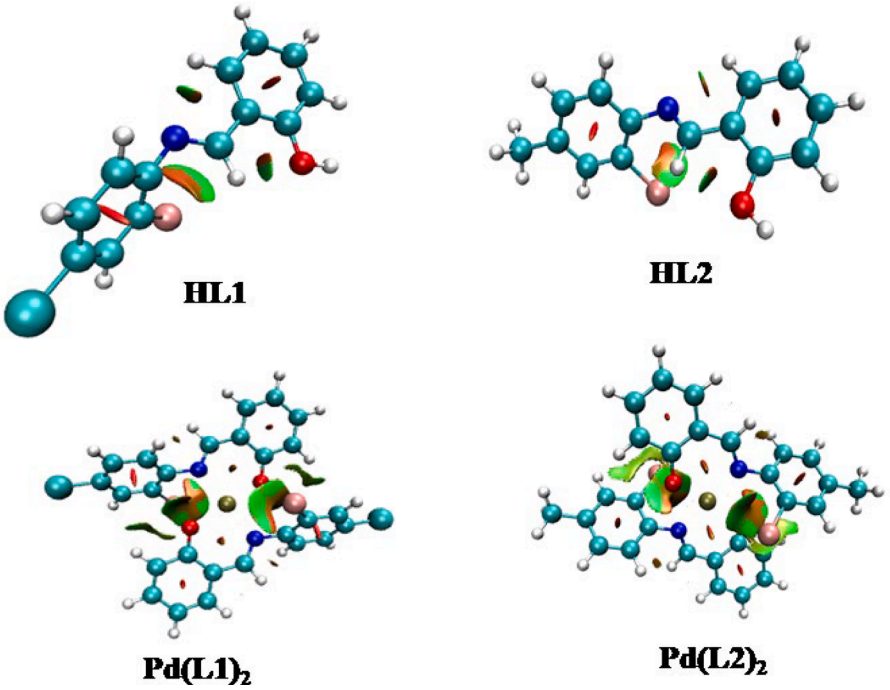

Fig. 13. Three dimensional non-covalent-interacting isosurfaces for ligands and their complexes.

toward these cell lines under the tested assay condition of 10 μgmL^{-1}.

4. Theoretical study

4.1. Non-covalent-interactions (NCI)

NCI is a method for analyzing intramolecular interactions such as van der Waals attractive forces, hydrogen bonding, and steric repulsions, and as well as their influence on the biological activity on a given compounds. It also provides qualitative and quantitative information about where these encounters distributions can occur. The locations in space where the reduced density gradient (RDG) on the y-axis is close to zero and creates well-defined troughs that provide information regarding electron densities (sign λ_2 (ρ)) of these interactions in two-dimensional NCI index analysis (Fig. 12). The RDG regions are known as isosurfaces, and they are distinguished by electron density, which is caused by tiny gradients along each of them. While van der Waals attractive forces are typically green, steric repulsions are typically red, and hydrogen bonding is typically blue. With bigger sign λ_2 (ρ) values, more intense colors imply stronger interactions [36]. When

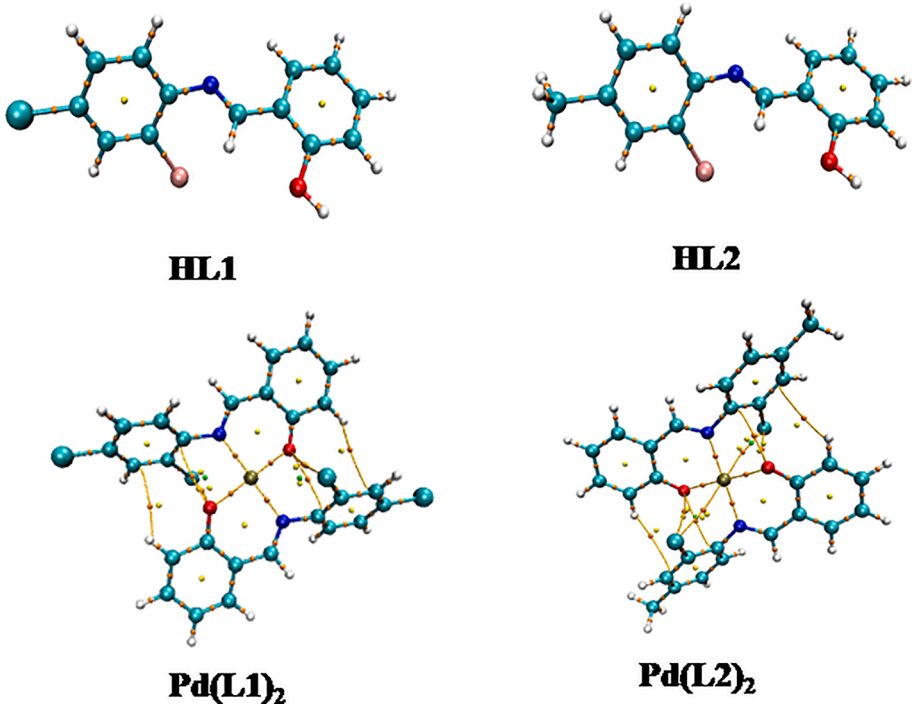

Fig. 14. Non-covalent-interacting atomic interaction lines and bond critical points for ligands and their complexes.

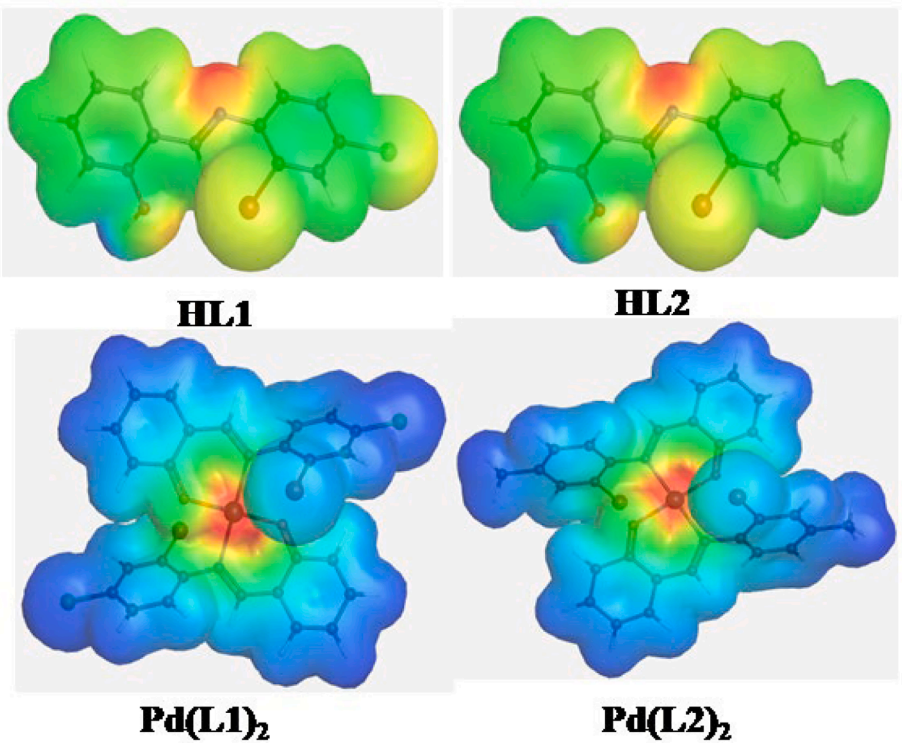

Fig. 15. Molecular electrostatic potentials on ligands and their complexes.

comparing **HL1** to **HL2**, the former has three well-defined troughs while the latter has only one. In **HL1**, there are two well-defined troughs result from steric repulsions, while one results from van der Waals attractive forces. A complete absence of van der Waals attractive forces in **HL2** is observed. Thus, the increased biological activity of **HL1** over **HL2** is justified owing to it stability due to the steric factors [77]. In comparing **HL1** to **Pd(L1)$_2$**, only one well-defined trough that results from steric repulsion is observed in the latter. Two well-defined troughs that result from very weak van der Waals attractive forces are also observed in this compound. However, relating **HL2** to **Pd(L2)$_2$**, we observe four well-defined troughs that result from van der Waals attractive forces in the latter. Amongst these, two stronger ones appear that were absent in **Pd(L1)$_2$** and two more well-defined troughs that result from steric repulsion also appear to be absent in both **HL2** and **Pd(L2)$_2$**. Due to the presence of multiple electron-withdrawing substituents on the aromatic ring, NCI dominates in **HL1** and **Pd(L1)$_2$** and promotes their biological activity over **HL2** and **Pd(L2)$_2$**. This is due to the fact that NCI promotes molecular recognition, protein stabilization, and efficient enzymatic

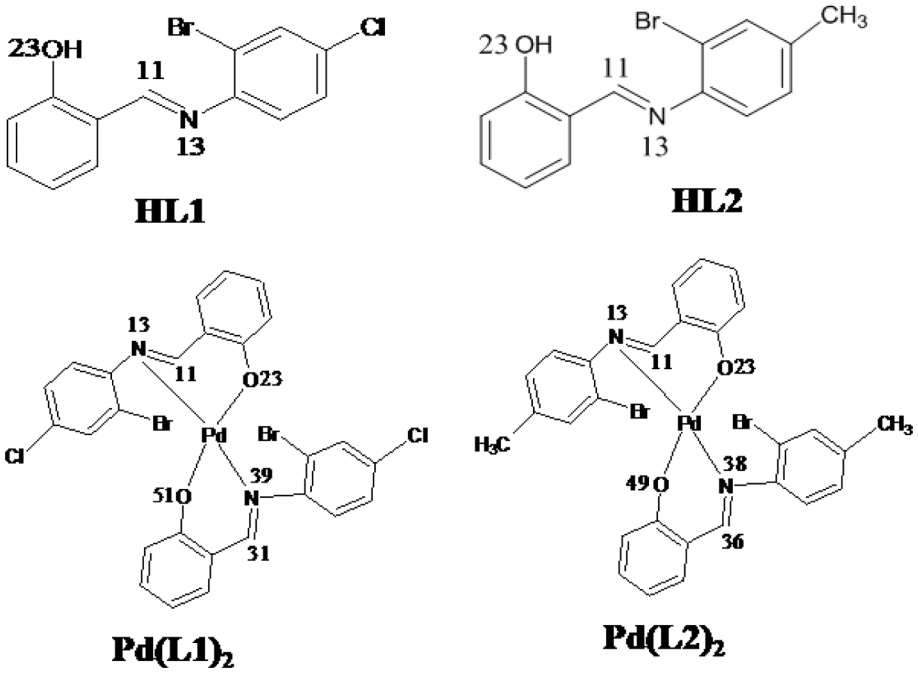

Fig. 16. Atomic numbering of atoms.

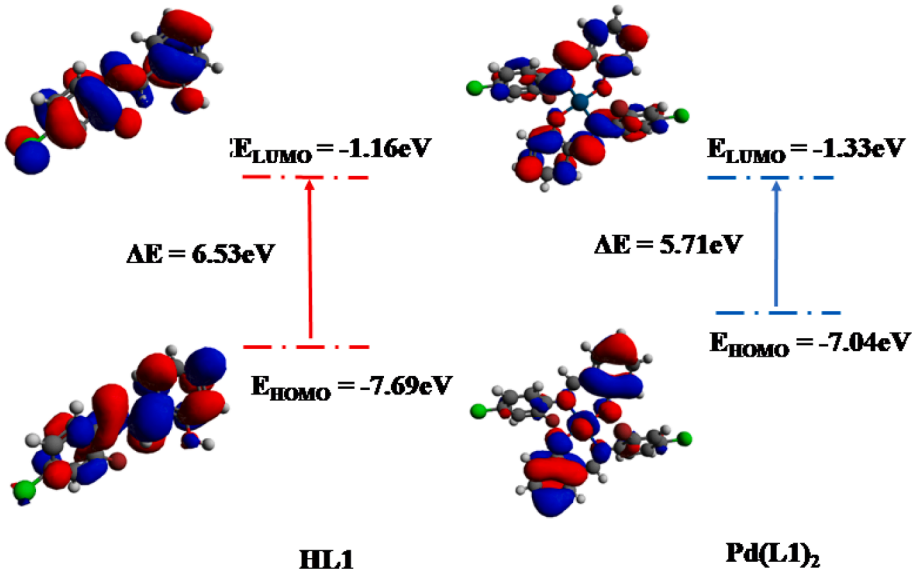

Fig. 17. The frontier molecular orbital of **HL1** and **Pd(L1)$_2$**.

reactions [78]. NCI and structural fitness are also important factors in biological activity [79]. In addition, because DNA is the primary target of anticancer drugs, and NCI allows aromatic rings stacked with electron-withdrawing groups to bind to DNA [80]. As a result, adding an electron-rich metal ion like palladium to a ligand system dominated by electron-withdrawing substituents like **HL1** increases biological activity, as seen with **Pd(L1)$_2$**.

Isosurfaces, which come in sheet, disc, and pill shapes, are commonly used to expose three-dimensional NCI (Fig. 13). The red pill-shaped isosurfaces in the center of each benzene ring represent ring closure, while the green and red sheets and disks represent van der Waals attractive and repulsive interactions, and blue disks represent hydrogen bonding [36]. The complexes' folded sheets provide evidence of intra-ligand and metal–ligand stabilizing interactions. Around these interactions, a multicentric buildup of electron density occurs, which stabilizes the chelate ring. The red color, i.e., the steric strain, which counterbalances the green part as steric crowding in the chelate ring induces instability [36], reveals more evidence of this multicentric build up. This explains the degree of homogeneous electron distribution within the molecules as the driving force behind the differences in biological properties exhibited by the ligands and their complexes. This supports Chakraborty's point about the role of NCI in Pd(II) complexes [81].

For the complexes, several atomic interaction lines (AIL) are detected, but none for the ligands (Fig. 14). These lines depict atom interaction routes. The electron densities on these contact routes are often measured *via* bond critical points (BCP) [34,82]. C…H, C…O, and Br…O interactions predominate in both complexes. This is to be expected due to the charge density sharing between the Pd(II) ion and the donor atoms [83].

4.1.1. Molecular electrostatic potential (MEP)

MEP is a chemical descriptor that analyzes electro negativities on compounds and generates an electron density map that depicts where an electrophilic or nucleophilic attack occurs [84]. Red images reveal the former, whereas blue images reveal the latter (Fig. 15). As a result, the potential decreases in the following order: blue > green > yellow > orange > red. In both ligands, the nitrogen atom of the imine moiety has a high concentration of electrons, whereas the hydrogen atom of the OH moiety has a low concentration of electrons. The oxygen atom of this OH moiety, as well as the halogens, has a high concentration of electrons. As a result, **HL1** has more electrons than **HL2**, which translates into their biological properties. This is what accounts for **HL1**′s higher biological activity when compared to **HL2**. Similar observation was reported by Majeed and co-workers [85]. The high concentration of electrons on the nitrogen atom of the imine moiety and the oxygen atom of the OH moiety is transferred to the metal center upon complexation. This provides a plausible explanation for the higher radical scavenging activity and better cytotoxicity activity that was observed earlier for the complexes than their respective ligands. The blue colors clearly show a decrease in electron concentrations on the ligands (Fig. 15), and this render them less biologically active. The donor atoms and the carbon atom from the imine moiety are depicted in Fig. 16. Table S5 shows quantitative values for the electron densities of these donor atoms and carbon atoms from imine moieties. A higher concentration of electrons is observed on C11 than on N13 in **HL1.** The inductive effect causes the 2, 6 substituted chloro and bromo groups to remove electrons from the aromatic ring, resulting in electron delocalization. This induces an electron flow from the nitrogen atom's lone pair electrons to stabilize the aromatic ring, resulting in a larger electron concentration on C11. In the instance of **HL2**, the inductive action causes the CH_3 moiety to contribute electrons into the aromatic ring. This induces a higher flow of electrons towards the nitrogen atom via delocalization, resulting in a drop in electron density on C11 and the stabilization of the imine moiety. The electron density on C11 and C37 falls considerably during complexation. This happens because the electron density of O23 and O51 decreases during bond formation. Due to the involvement their lone pairs of electrons in the bond formation, the electron density of N13 and N39 decreases. **Pd(L2)$_2$** has a similar set of effects.

4.1.2. Conceptual density functional theory (CDFT)

CDFT is another chemical descriptor that helps locate reactive regions in compounds. CDFT, unlike MEP, can detect potential places for radical attacks. It can measure ionization potential (IP), electron affinities (EA), hardness, softness, electrophilicity indices, nucleophilicity indices, and chemical potentials, among other things (Table S6). In addition, it also provides information that supports the biological properties of compounds [86]. Radical attacks show atomic locations capable of absorbing reactive oxygen species (ROS) and rendering them inactive, and function as potential radical scavenger for antioxidant study as seen from the complexes. This can help in evaluating structure–activity relationships during molecular docking analyses through identification of potential binding site. Although it is commonly assumed that an electron in the highest occupied molecular orbital

Table 5
The binding affinity and the amino acid residues involved in the interaction of the compounds with the biological targets.

Protein	Ligands	Binding energy ($kcalmol^{-1}$)	Bonding interactions
3EQM	HL1	−7.0	Leu152, Met303, Ala306, Ala307, Met364, Val370, Cys437, Phe430, Gly439, Ala443
	HL2	−7.2	Arg115, Ile133, Phe148, Ala306, Val373, Ala438,
	Pd(L1)2	−9.8	Ile132, Ile133, Trp141, Phe148, Leu152, Met303, Ala306, Thr310, Val370, Cys437, Ala438
	Pd(L2)2	−10.0	Ile132, Ile133, Phe148, Leu152, Ala306, Thr310, Val370, Cys437, Ala438
	5-Fluorouracil	−5.4	Phe21, Asp309, Val313, Ser478, His480
	Co-ligand	−8.4	Arg145, Ala438
2W3L	HL1	−6.4	Ala59, Asp62, Phe63, Val107, Tyr161
	HL2	−6.6	Ala59, Asp62, Phe63, Val107, Tyr161
	Pd(L1)2	−10.2	Arg65, Arg66, Tyr67, Arg68, Ala72
	Pd(L2)2	−10.3	Arg65, Arg66, Arg68, Ala72
	5-Fluorouracil	−4.6	Lys22, Arg26, Phe71, Ser75, Val115, Val118
	Co-ligand	−9.3	Arg26, Arg66, Ala72, Asn102, Val107, Val115, Val118, Glu119, Tyr161

(HOMO) will be automatically excited to the lowest unoccupied molecular orbital (LUMO), a recent study by Bulat *et al.* revealed that the molecule's contour and an electron's position in atomic space also plays a role in excitations. In fact, when they studied twelve compounds, they discovered that electrons in only five of the twelve that inhabited the HOMO level were excited to the LUMO level [87]. Nonetheless, it is widely acknowledged that HOMO-LUMO energy gaps are important in understanding the chemical stability and reactivity of many organic compounds [38]. Compounds with high HOMO-LUMO energy gaps are more stable and less reactive and those with lower energy gap more reactive [88], as HOMO-LUMO energy gaps are directly related to ionization potential (IP) and electron affinity (EA). The complexes exhibit lower HOMO-LUMO energy gaps than the ligands (Figs. 16–17), resulting in lower IP and higher EA. This provides a plausible explanation for the enhanced radical scavenging and greater inhibition cytotoxicity activities for the complexes. Because they are softer than ligands, and their electrophilicity indices are higher. The electrophilic index is an essential indicator for the chemical toxicity and reactivity of a given compound. It is used to measure the pharmacological activity of drug-receptor interaction [89]. Hence, the higher value obtained for the complexes compared to their ligands further support the biological activity displayed by the complexes over the ligands. Similarly, the nucleophilicity index of the complexes (4.84 eV) was found to be higher than their ligands (3.18–3.43) eV, indicating nucleophilic complexes. This is typical of d^8 square planar complexes of Pd(II) and Pt(II), due to their electron rich nature. Nucleophilic complexes are known to be biologically viable owing to their ability to undergo changes in both oxidation state and coordination number, which allows them to perform a number of important roles [90]. This agrees with the results of antioxidant and cyto-toxicity studies.

To measure local quantities for the reactivity/selectivity on atomic sites of a molecule, CDFT uses a chemical descriptor called the Fukui Function. It is defined as follows.

$$f(\vec{r}) = \frac{\partial \rho}{\partial N} v(\vec{r}) = \left(\frac{\delta \mu}{\delta v \vec{r}}\right) N \quad (1)$$

Table S7 contains the Hirshfeld charges (q), condensed Fukui Functions (f, f^+ and f^0) and charge density difference (CDD). The following equations can be used to calculate the Fukui Function.

$f^+(\vec{r}) = q_r(N+1) - q_r(N)$ (2)

For a nucleophilic attack

$$f^-(\vec{r}) = q_r(N) - q_r(N-1) \quad (3)$$

For an electrophilic attack

$$f^0(\vec{r}) = q_r(N+1) - q_r(N-1) \quad (4)$$

For a radical attack

The charge density difference (CCD) is the difference between $f^+(\vec{r})$ and $f^-(\vec{r})$ [91]. In **HL1**, it is observed that there is a high probability for a nucleophilic attack on C11 with a high probability for a radical attack also. An even higher probability for a radical attack is observed on N13. A similar scenario is observed in **HL2**. Upon complexation to produce **Pd(L1)$_2$**, the probability for a radical attack on N39 is enhanced. A slight enhancement for a radical attack on N13 in **Pd(L2)$_2$** is observed also. This provides a plausible explanation for the enhanced radical scavenging and greater cytotoxicity inhibition activities that were observed in the complexes.

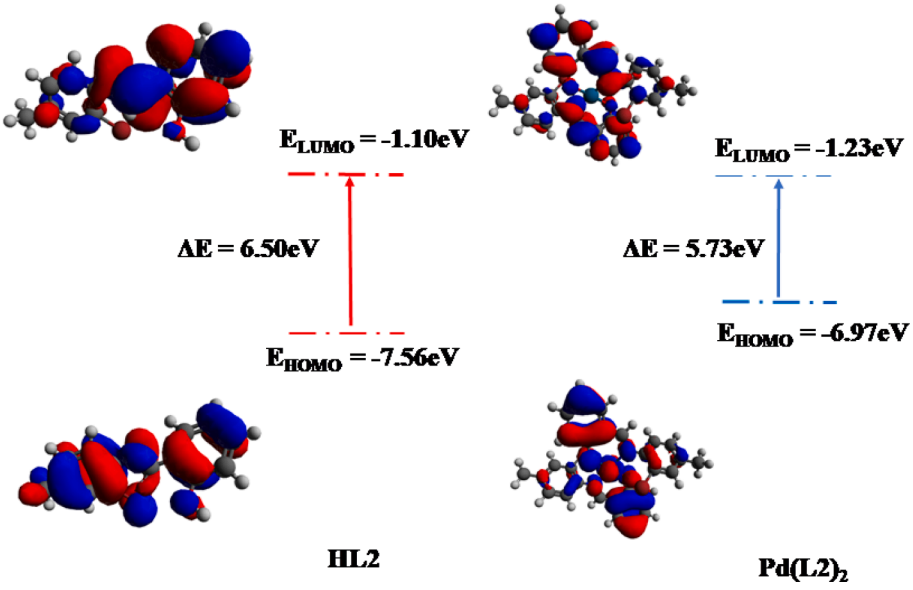

Fig. 18. The frontier molecular orbital of **HL2** and **Pd(L2)$_2$**.

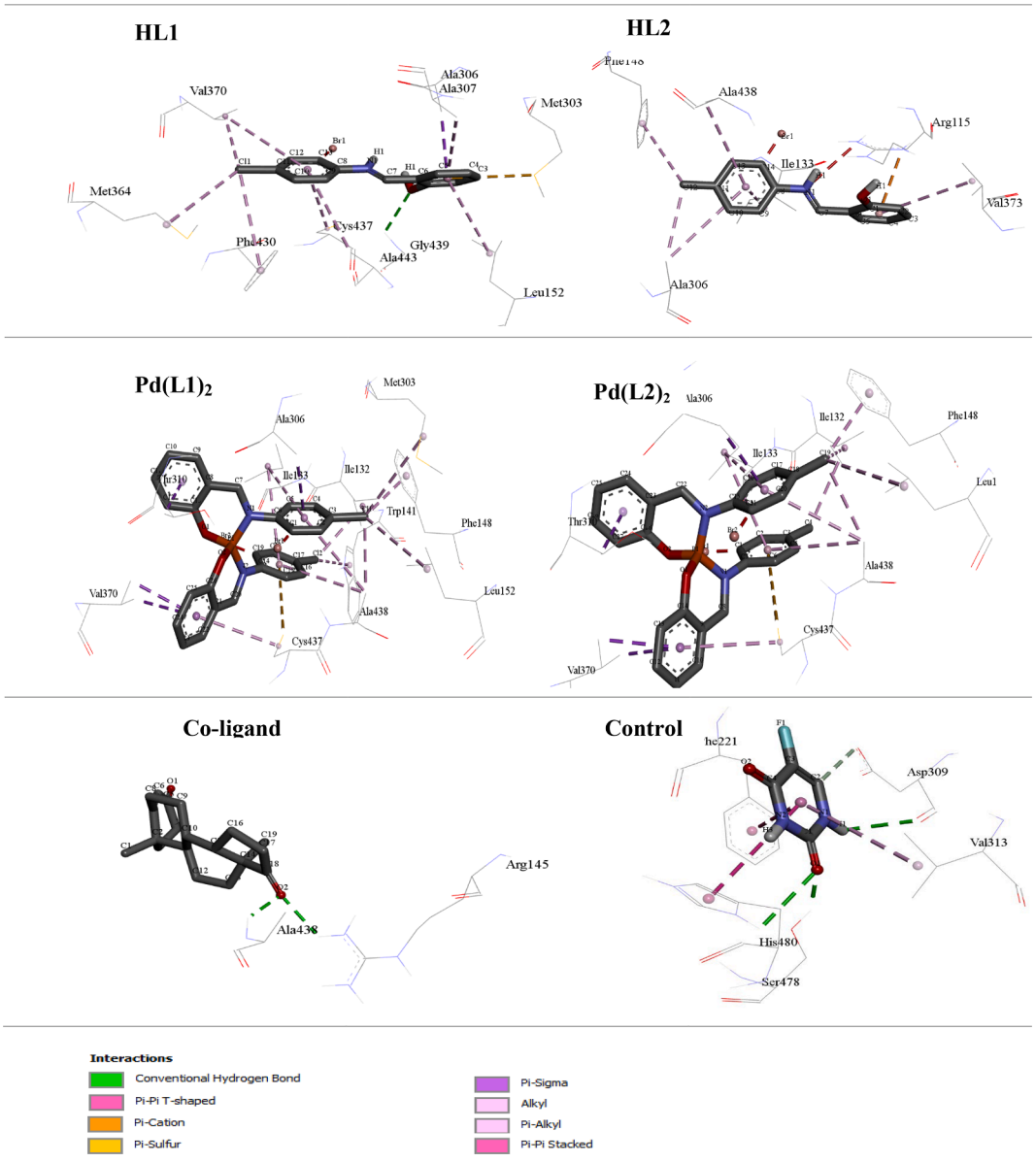

Fig. 19. 3D interactions of the compounds, co-crystallized ligand, and the standard drug 5-fluorouracil within the active site region of3EQM.

4.2. Molecular docking study

Molecular docking calculations were performed to establish the conformation and binding ability of the synthesized compounds in the active sites of therapeutic targets 3EQM and 2W3L for human breast cancer and colon cancer cell lines. The docking results were compared to 5-fluorouracil and their respective co-crystallized ligands. According to the ranking produced by the scoring functions, which are shown in Table 5, the least among all estimated binding energies exhibited the highest activity. With a difference of 0.2 and 0.1 kcalmol^{-1} for 3EQM and 2W3L, respectively, the compounds **Pd(L1)$_2$** and **Pd(L2)$_2$** demonstrated comparable and highest binding affinities for both targets (Table 5). A similar result was obtained for **HL1** and **HL2**, establishing their interactions with both proteins with a difference of 0.2 kcalmol^{-1} in their binding energies. The co-crystallized ligand in the active site pockets of 3EQM and 2W3L demonstrated good binding energies of −8.4 and −9.3 kcalmol^{-1}, respectively. These binding energies are much better than those released by the interactions of the standard drug 5-fluorouracil with each of the therapeutic targets (Table 5).

The 3D representations of the binding modes and interactions of the compounds within the active site region of the MCF-7 protein target are displayed in Fig. 18. Compound **HL1** interacts with the 3EQM target to form 8 hydrophobic bonds (2 alkyl and 6 pi-alkyl bonds), 1 conventional hydrogen bond and 1 pi-sulphur bond. However, in compound **HL2**, only 6 pi-alkyl and1 pi-cation bonds were involved in the interactions. The compounds **Pd(L1)$_2$** and **Pd(L2)$_2$** revealed 4 pi-sigma, and 1 pi-sulphur bond interactions, they also established at least 11 hydrophobic interactions including 5 alkyl and 6 pi-alkyl bonds. The co-crystallized ligand has only 2 hydrogen bond interactions with Arg145 and Ala438 residues of the protein. The standard 5-fluorouracil showed 1 pi-alkyl interaction with Val313, 1 pi-pi stacked interaction with Phe221, 1 pi-pi T shaped interaction with His480, and 3 conventional hydrogen bond interactions with Asp309, Ser478 and His480.

The binding behavior of the compounds in the active site of the target protein 2W3L is presented in Fig. 19. **HL1** and **HL2** showed 1 alkyl bond interaction involving Ala59, as well as 2 pi-alkyl bond interactions with Val107 and Tyr161. The compounds also interacted with Phe62 and Asp63 to produce amide pi-stacked and pi-pi *T*-shaped bond interactions, respectively. The compound **Pd(L1)$_2$** produced 2 hydrogen bonding interactions withTyr67 and Arg68 of the protein. In addition,

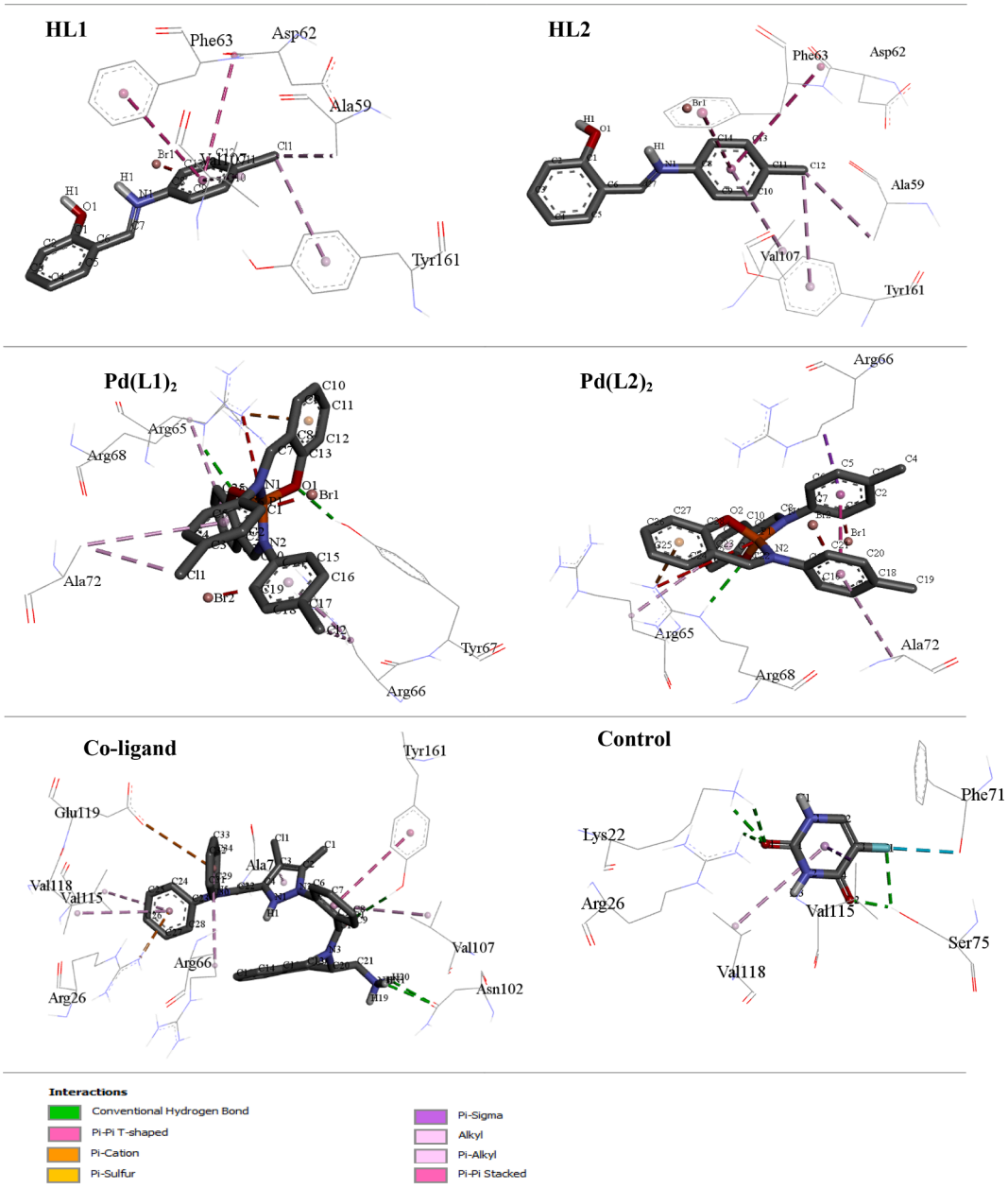

Fig. 20. 3D interactions of the compounds, co-crystallized ligand, and the standard drug 5-fluorouracil within the active site region of 2W3L.

the compound also established 1 pi-cation interaction with Arg68 as well as 5 alkyl bond interactions via theArg65, Arg 66, and Ala72 residues of the protein. Apart from the conventional hydrogen bonding interactions between **Pd(L2)$_2$** and Arg68, both Arg65 and Ala72 interacts with the compound to form pi-alkyl bond, Arg66 produce pi-sigma bond while a pi-cation bond was also released between the compound and Arg68. The docking results also indicated that the co-crystallized ligand in 2W3L formed 3 hydrogen bond interactions with Asn102 and Tyr161. Other bonding interactions consisting of 5 hydrophobic bonds (5 pi-alkyl bond) and 2 pi-cation and 2 pi-pi *T*-shaped interactions are also established within the active site pocket of the protein. Finally, the standard drug 5-fluorouracil showed 5 hydrogen bonds with Lys22, Arg26, and Ser75. The residues Phe71, Val115, and Val118 also established a halogen, pi-alkyl, and pi-sigma bond interactions with the drug molecule.Fig. 20.

5. Conclusion

Two palladium (II) complexes derived from *ON* bidentate (*Z*)-2-(phenylimino)methyl)phenol derivatives have been synthesized and characterized by various spectroscopic and analytical techniques. The geometry of the complexes was found to be square planar in which two ligand molecules coordinated to Pd(II) ion through nitrogen and oxygen atoms of the imine and phenolate groups. This coordination mode is further supported by the crystal structures of the complexes. The complexes show higher DPPH radical scavenging than the ligands, with **Pd(L1)$_2$** demonstrating more radical scavenging activity than **Pd(L2)$_2$**. Similarly, both complexes displayed enhanced cyto-toxic effect on breast cancer cell line MCF-7 and colon cancer HT-29 than the ligands with **Pd(L2)$_2$** taking the lead on all the cell lines. Furthermore, the complexes demonstrated less toxicity effect on (HepG-2 liver cell line) at lower concentration with cell viability of 70–80%. also, to understand the electronic and molecular properties of the compounds, DFT calculations and Hirshfeld surface analysis has been deduced. The results of

theoretical investigations correlate well with the experimental results and unveiled electronic properties that supported the biological activities displayed by the complexes and their ligands. Molecular docking study was performed to understand the behavior of the compounds within the active site pockets of the MCF-7 and H-29 proteins. The result shows **Pd(L1)$_2$** and **Pd(L2)$_2$** established significantly better and stronger conformational fittings within the active sites of the proteins than their ligands and control.

Declaration of Competing Interest

The authors declare that they have no known competing financial interests or personal relationships that could have appeared to influence the work reported in this paper.

Data availability

Data will be made available on request.

Acknowledgement

Dr TL Yusuf is grateful to Faculty of Science, University of Johannesburg for the award of a postdoctoral fellowship. We are also grateful to center for high performance computing for computational resources.

Appendix A. Supplementary data

Supplementary data to this article can be found online at https://doi.org/10.1016/j.ica.2023.121505.

References

[1] A. Budreviciute, S. Damiati, D.K. Sabir, K. Onder, P. Schuller-Goetzburg, G. Plakys, A. Katileviciute, S. Khoja, R. Kodzius, Front. Public Health (2020) 788.
[2] G.A. Roth, G.A. Mensah, C.O. Johnson, G. Addolorato, E. Ammirati, L.M. Baddour, N.C. Barengo, A.Z. Beaton, E.J. Benjamin, C.P. Benziger, J. Am. Coll. Cardiol. 76 (2020) 2982.
[3] H. Nagai, Y.H. Kim, J. Thorac. Dis. 9 (2017) 448.
[4] P.D. Le, C. Taylor, A. Cabanes, H.T.T. Tran, Support. Care Cancer 30 (2022) 9.
[5] C.-H. Chen, Y. Jiang, R. Wu, Y. Tang, C. Wan, H. Gao, Z. Mao, Bioorg. Med. Chem. Lett. 48 (2021), 128233.
[6] M. Hallek, Am. J. Hematol. 94 (2019) 1266.
[7] O. Ginsburg, F. Bray, M.P. Coleman, V. Vanderpuye, A. Eniu, S.R. Kotha, M. Sarker, T.T. Huong, C. Allemani, A. Dvaladze, Lancet 389 (2017) 847.
[8] F.K. Camellia, M. Ashrafuzzaman, M.N. Islam, L.A. Banu, M. Kudrat-E-Zahan.
[9] L.H. Abdel-Rahman, M.S.S. Adam, N. Al-Zaqri, M.R. Shehata, H.-E.-S. Ahmed, S. K. Mohamed, Arab. J. Chem. 15 (2022), 103737.
[10] S. Daravath, A. Rambabu, N. Ganji, G. Ramesh, P.A. Lakshmi, J. Mol. Struct. 1249 (2022), 131601.
[11] S. Sen, N. Chowdhury, T.-W. Kim, M. Paul, D. Debnath, S. Jeon, A. Bagchi, J. Im, G. Biswas, Bioinorg. Chem. Appl. 2022 (2022).
[12] L.H. Abdel-Rahman, M.T. Basha, B.S. Al-Farhan, M.R. Shehata, E.M. Abdalla, Appl. Organomet. Chem. 36 (2022) e6484.
[13] S.D. Oladipo, T.L. Yusuf, S.J. Zamisa, G.F. Tolufashe, K.A. Olofinsan, Z. Tywabi-Ngeva, N. Mabuba, Eur. J. Chem. 12 (2021) 204.
[14] S. Mbugua, N. Sibuyi, L. Njenga, R. Odhiambo, S. Wandiga, M. Meyer, New Palladium (II) and Platinum (II) complexes based on pyrrole schiff bases: synthesis, characterization, X-ray structure, and anticancer activity, ACS Omega 5 (2020) 14942–14954.
[15] A. Şenocak, H. Akbaş, Cumhuriyet Sci. J. 42 (2021) 68.
[16] P. Kavitha, K.L. Reddy, Arab. J. Chem. 9 (2016) 640.
[17] L.E. Sarto, E.P. De Gois, G.G. De Andrade, M.S. De Almeida, J.T.J. Freitas, A.D.S. R. Júnior, L.P. Franco, C. Torres, E.T. De Almeida, C.M.C.P. Gouvêa, Anticancer Res 39 (2019) 6693.
[18] T.L. Yusuf, D.C. Akintayo, S.D. Oladipo, A.A. Adeleke, K. Olofinsan, B. Vatsha, N. Mabuba, New J. Chem. 46 (2022) 12968.
[19] T.L. Yusuf, S.D. Oladipo, S.A. Olagboye, S.J. Zamisa, G.F. Tolufashe, J. Mol. Struct. 1222 (2020), 128857.
[20] S. Sharma, R. Meena, R. Singh, N. Fahmi, Main Group Met. Chem. 39 (2016) 31.
[21] M. Ariyaeifar, H.A. Rudbari, M. Sahihi, Z. Kazemi, A.A. Kajani, H. Zali-Boeini, N. Kordestani, G. Bruno, S. Gharaghani, J. Mol. Struct. 1161 (2018) 497.
[22] K. Buldurun, N. Turan, A. Savcı, N. Colak, J. Saudi Chem. Soc. 23 (2019) 205.
[23] I. Waziri, T.L. Yusuf, E. Akintemi, M.T. Kelani, A. Muller, J. Mol. Struct. (2022), 134382.
[24] I. Waziri, M.T. Kelani, M.O. Oyedeji-Amusa, A.K. Oyebamiji, L.-C.-C. Coetzee, A. S. Adeyinka, A.J. Muller, J. Mol. Struct. 1276 (2023), 134756.
[25] M. Sunjuk, L. Al-Najjar, M. Shtaiwi, B. El-Eswed, M. Al-Noaimi, L. Al-Essa, K. Sweidan, Inorganics 10 (2022) 43.
[26] M.M.S. Saif, R.M. Alodeni, A.A. Alghamdi, A.-B. Al-Odayni, J. King Saud Univ.-Sci. 34 (2022), 101988.
[27] B.S. Al-Farhan, M.T. Basha, L.H. Abdel Rahman, A.M. El-Saghier, D. Abou El-Ezz, A.A. Marzouk, M.R. Shehata, E.M. Abdalla, Molecules 26 (2021) 4725.
[28] C.B. Pinto, B.L. Rodrigues, L.H. Dos Santos, J. Appl. Cryst. 54 (2021).
[29] E. Bursal, F. Turkan, K. Buldurun, N. Turan, A. Aras, N. Çolak, M. Murahari, M. C. Yergeri, Biometals 34 (2021) 393.
[30] Y. Zhao, D.G. Truhlar, Theor. Chem. Acc. 120 (2008) 215.
[31] P.J. Hay, W.R. Wadt, J. Chem. Phys. 82 (1985) 299.
[32] M. Frisch, G.W. Trucks, H.B. Schlegel, G.E. Scuseria, M.A. Robb, J.R. Cheeseman, G. Scalmani, V. Barone, B. Mennucci, G. Petersson, Gaussian 09, revision D. 01. Gaussian, Inc., Wallingford CT, 2009.
[33] E. Cances, B. Mennucci, J. Tomasi, J. Chem. Phys. 107 (1997) 3032.
[34] T. Lu, F. Chen, J. Theor. Comput. Chem. 11 (2012) 163.
[35] W. Humphrey, A. Dalke, K. Schulten, J. Mol. Graph. 14 (1996) 33.
[36] R. Chaudret, B. De Courcy, J. Contreras-Garcia, E. Gloaguen, A. Zehnacker-Rentien, M. Mons, J.-P. Piquemal, PCCP 16 (2014) 9876.
[37] I. Kostova, N. Trendafilova, G. Momekov, J. Inorg. Biochem. 99 (2005) 477.
[38] H. AlRabiah, S. Muthu, F. Al-Omary, A.-M. Al-Tamimi, M. Raja, R.R. Muhamed, A.-A.-R. El-Emam, Maced. J. Chem. Chem. Eng. 36 (2017) 59.
[39] H. Berman, K. Henrick, H. Nakamura, Nat. Struct. Mol. Biol. 10 (2003) 980.
[40] N.M. O'Boyle, M. Banck, C.A. James, C. Morley, T. Vandermeersch, G. R. Hutchison, J. Cheminf. 3 (2011) 1.
[41] T. Khan, A.J. Lawrence, I. Azad, S. Raza, A.R. Khan, JSM Chemistry 6 (2018) 1053.
[42] G.M. Morris, D.S. Goodsell, R.S. Halliday, R. Huey, W.E. Hart, R.K. Belew, A. J. Olson, J. Comput. Chem. 19 (1998) 1639.
[43] R. Satheeshkumar, J. Wu, R. Chandrasekaran, K. Revathi, H.A. Sparkes, W.-L. Wang, Appl. Organomet. Chem. 34 (2020) e5856.
[44] Z. Faghih, A. Neshat, A. Wojtczak, Z. Faghih, Z. Mohammadi, S. Varestan, Inorg. Chim. Acta 471 (2018) 404.
[45] J. Dutta, M.G. Richmond, S. Bhattacharya, Dalton Trans. 44 (2015) 13615.
[46] L.E. Sarto, W.P.D. Badaró, E.P. de Gois, M.I.F. Barbosa, C. Torres, R.B. Viana, J. Honorato, E.E. Castellano, E.T. de Almeida, J. Mol. Struct. 1204 (2020), 127549.
[47] G. Lupaşcu, E. Pahonţu, S. Shova, Ş.F. Bărbuceanu, M. Badea, C. Paraschivescu, J. Neamţu, M. Dinu, R.V. Ancuceanu, D. Drăgănescu, C.E. Dinu-Pîrvu, Appl. Organomet. Chem. 35 (2021) e6149.
[48] S. Mahato, P. Rawal, A.K. Devadkar, M. Joshi, A. Roy Choudhury, B. Biswas, P. Gupta, T.K. Panda, Org. Biomol. Chem. 20 (2022) 1103.
[49] J. Sanmartín-Matalobos, A. García-Deibe, M. Zarepour-Jevinani, M. Aboal-Somoza, P. Bermejo-Barrera, M. Fondo, Crystals 10 (2020) 235.
[50] D. Sharma, H. Revanasiddappa, Current Chemistry Letters 8 (2019) 39.
[51] C. Mchiri, L.-C.-C. Coetzee, F. Chandoul, A. Jedidi, A.S. Adeyinka, N. Magwa, T. Roisnel, S. Ben Moussa, H. Nasri, Molecules 27 (2022) 3833.
[52] D. Majumdar, A. Frontera, R.M. Gomila, S. Das, K. Bankura, RSC Adv. 12 (2022) 6352.
[53] G.F. Bozza, R.L. de Farias, R.F. de Souza, F.V. Rocha, C.V. Barra, V.M. Deflon, E. T. de Almeida, A.E. Mauro, A.V. Netto, J. Mol. Struct. 1175 (2019) 195.
[54] C. Feng, X.-J. Li, D. Zhang, Z.-R. Qu, H. Zhao, J. Iran. Chem. Soc. 13 (2016) 823.
[55] N. Özdemir, M. Kaloğlu, N. Kaloğlu, N. Gürbüz, İ. Özdemir, Inorg. Nano-Metal Chem. 52 (2022) 493.
[56] B. Jeziorski, R. Moszynski, K. Szalewicz, Chem. Rev. 94 (1994) 1887.
[57] R. Tiwari, M. Nath, New J. Chem. 39 (2015) 5500.
[58] J. Shelnutt, V. Ortiz, J. Phys. Chem. 89 (1985) 4733.
[59] K. Nakamoto, Infrared and Raman Spectra of Inorganic and Coordination Compounds, Part B: Applications In Coordination, Organometallic, And Bioinorganic Chemistry, John Wiley & Sons, 2009.
[60] A.N. Rosnizam, M.A. Hamali, A.L.M. Low, H.M. Youssef, H. Bahron, A.M. Tajuddin, J. Mol. Struct. 1260 (2022), 132821.
[61] R.H. Rajegowda, R.P. Kumar, B. Das, J. Coord. Chem. 75 (2022) 1273.
[62] K.C. Gupta, A.K. Sutar, Coord. Chem. Rev. 252 (2008) 1420.
[63] H. Kargar, M. Fallah-Mehrjardi, R. Behjatmanesh-Ardakani, M. Bahadori, M. Moghadam, M. Ashfaq, K.S. Munawar, M.N. Tahir, Polyhedron 213 (2022), 115622.
[64] T. Mahamo, M.M. Mogorosi, J.R. Moss, S.F. Mapolie, J.C. Slootweg, K. Lammertsma, G.S. Smith, J. Organomet. Chem. 703 (2012) 34.
[65] N. Kordestani, H.A. Rudbari, I. Correia, A. Valente, L. Côrte-Real, M.K. Islam, N. Micale, J.D. Braun, D.E. Herbert, N. Tumanov, New J. Chem. 45 (2021) 9163.
[66] H.A. Mohamad, K.O. Ali, T.A. Gerber, E.C. Hosten, Bull. Chem. Soc. Ethiop. 36 (2022) 617.
[67] V. Nagalakshmi, M. Sathya, M. Premkumar, D. Kaleeswaran, G. Venkatachalam, K. Balasubramani, J. Organomet. Chem. 914 (2020), 121220.
[68] S. Munusamy, P. Muniyappan, V. Galmari, J. Coord. Chem. 72 (2019) 1910.
[69] L.F. Dechouk, A. Bouchoucha, Y. Abdi, K.S. Larbi, A. Bouzaheur, S. Terrachet-Bouaziz, J. Mol. Struct. 1257 (2022), 132611.
[70] M. Krause, R. von der Stück, D. Brünink, S. Buss, N.L. Doltsinis, C.A. Strassert, A. Klein, Inorg. Chim. Acta 518 (2021), 120093.
[71] D. Anu, P. Naveen, N.P. Rath, M. Kaveri, J. Mol. Struct. 1206 (2020), 127703.
[72] S. Moosun, M. Bhowon, E. Hosten, S. Jhaumeer-Laulloo, J. Coord. Chem. 69 (2016) 2736.
[73] S. Tetteh, D.K. Dodoo, R. Appiah-Opong, I. Tuffour, J. Inorg. Chem. 2014 (2014).
[74] Q.U. Ain, U. Ashiq, R.A. Jamal, M. Mahrooof-Tahir, Spectrochim. Acta A Mol. Biomol. Spectrosc. 115 (2013) 683.
[75] N. Ahmad, E.H. Anouar, A.M. Tajuddin, K. Ramasamy, B.M. Yamin, H. Bahron, PLoS One 15 (2020) e0231147.

[76] K.A. Abu-Safieh, A.S. Abu-Surrah, H.D. Tabba, H.A. AlMasri, R.M. Bawadi, F. M. Boudjelal, L.H. Tahtamouni, J. Chem. 2016 (2016).
[77] E. Broclawik, T. Borowski, M. Radoń, Transition Metals in Coordination Environments: Computational Chemistry and Catalysis Viewpoints, Springer, 2019.
[78] O. Yamauchi, Phys. Sci. Rev. 1 (2016).
[79] B.M. Zeglis, V.C. Pierre, J.K. Barton, Chem. Commun. (2007) 4565.
[80] H.-K. Liu, P.J. Sadler, Acc. Chem. Res. 44 (2011) 349.
[81] J. Chakraborty, Heliyon (2022) e11408.
[82] T. Lu, Q. Chen, Acta Physicochim. Sinica 34 (2018) 503.
[83] R.F. Bader, H. Essén, J. Chem. Phys. 80 (1984) 1943.
[84] C.H. Suresh, G.S. Remya, P.K. Anjalikrishna, Wiley Interdiscip. Rev.: Comput. Mol. Sci. (2022) e1601.
[85] S.R. Majeed, M.A. Amin, F.A. Attaby, M.E. Alberto, A.A. Soliman, Molecules 27 (2022) 964.
[86] S.A. Khan, K. Rizwan, S. Shahid, M.A. Noamaan, T. Rasheed, H. Amjad, Appl. Organomet. Chem. 34 (2020) e5444.
[87] P. Politzer, K.E. Riley, F.A. Bulat, J.S. Murray, Comput. Theor. Chem. 998 (2012) 2.
[88] M. Miar, A. Shiroudi, K. Pourshamsian, A.R. Oliaey, F. Hatamjafari, J. Chem. Res. 45 (2021) 147.
[89] A.M. Fahim, H.S. Magar, N.H. Mahmoud, Appl. Organomet. Chem. 36 (2022) e6616.
[90] C. Parks, University of Sheffield, 2015.
[91] P. Thanikaivelan, J. Padmanabhan, V. Subramanian, T. Ramasami, Theor. Chem. Acc. 107 (2002) 326.